Total Internal Reflection Spectroscopy for Studying Soft Matter

David A. Woods[1,2,a] and Colin D. Bain[2,b]

[1] *Formerly at:* Department of Physics, University of Exeter, Stocker Road, Exeter, UK, EX4 4QL.
[2] Department of Chemistry, Durham University, South Road, Durham, UK, DH1 3LE.
[a] E-mail: david.woods@durham.ac.uk
[b] E-mail: c.d.bain@durham.ac.uk

7th November 2013

Abstract

Total internal reflection (TIR) spectroscopy is a widely used technique to study soft matter at interfaces. This tutorial review aims to provide researchers with an overview of the principles, experimental design and applications of TIR spectroscopy to enable them to understand how this class of techniques might be used in their research. It also highlights limitations and pitfalls of TIR techniques, which will assist readers in critically analysing the literature. Techniques covered include attenuated total reflection infrared spectroscopy (ATR-IR), TIR fluorescence, TIR Raman scattering and cavity-enhanced techniques. Other related techniques are briefly described.

Contents

# 1 Introduction

Interfaces play a central role in many aspects of soft matter: for example, surfactants adsorb to interfaces, lipid bilayers enclose cells and organelles, any phase-separation process involves the formation an interface, the surfaces of polymers (and other materials) have different structures and properties from the bulk, and the stability of sols, foams and emulsions is dependent

on interfacial properties. Spectroscopy of interfaces is key to identifying the chemical nature, conformation and orientation of molecules at an interface, and to quantifying the composition of an interfacial film. The central challenge in interfacial spectroscopy is distinguishing the few molecules at the interface from the much greater number of molecules in the bulk. There are two main approaches to achieving surface selectivity. The first is to use a form of spectroscopy where the selection rules—arising from the symmetry of the molecular transitions—mean that only molecules at an interface can be detected. Second-order nonlinear optical techniques, such as sum-frequency generation and second harmonic generation, vanish in centrosymmetric media but are permitted at interfaces, which break the inversion symmetry of (most) bulk phases. The disadvantage of the selection rule-based approach is that nonlinear optical techniques are experimentally demanding (in sum-frequency generation two pulsed lasers of different wavelengths must be delivered to the sample simultaneously) and can be difficult to interpret. Furthermore, molecules at an interface that do not have a preferred orientation are invisible in second-order nonlinear spectroscopy, so such techniques are of limited value for quantitative analysis of composition. The second approach is to use optical methods to restrict the excitation light to the interface (or alternatively, to collect only light emitted from the interface). The total internal reflection spectroscopic techniques reviewed here fall into this category, as do external reflection infrared and waveguide spectroscopy, and near-field microscopy. Also in this category is surface enhanced Raman scattering (SERS), where the excitation of a surface plasmon in a metal generates an electric field that decays very rapidly with distance from the surface.[1,2]

In total internal reflection spectroscopy, the probe light is delivered to an interface through the more optically dense material at an angle of incidence greater than the *critical angle*. When light passes from a material with high refractive index to one with low refractive index it is refracted so that the angle of the transmitted light to the surface normal is greater than the angle of the incident light. Above a certain angle of incidence (the critical angle) there is no possible angle of refraction and all the light is reflected from the interface. Maxwell's equations require that the components of the electric and magnetic field vectors parallel to the interface must be continuous across the interface*—so a small amount of light must penetrate into the lower refractive index medium: this light is termed the *evanescent wave*. Figure 1 illustrates the concept of total internal reflection (TIR). The mathematics of the evanescent wave is discussed in more detail later in this review.
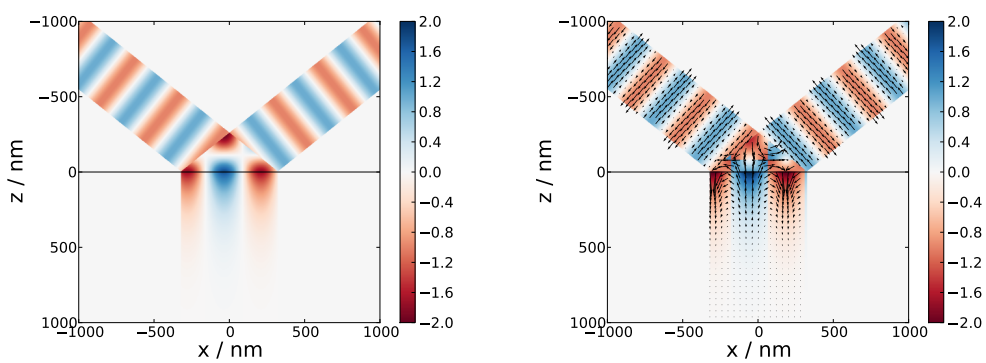
---

*The magnetic field vector is only continuous across the interface in the absence of a current.
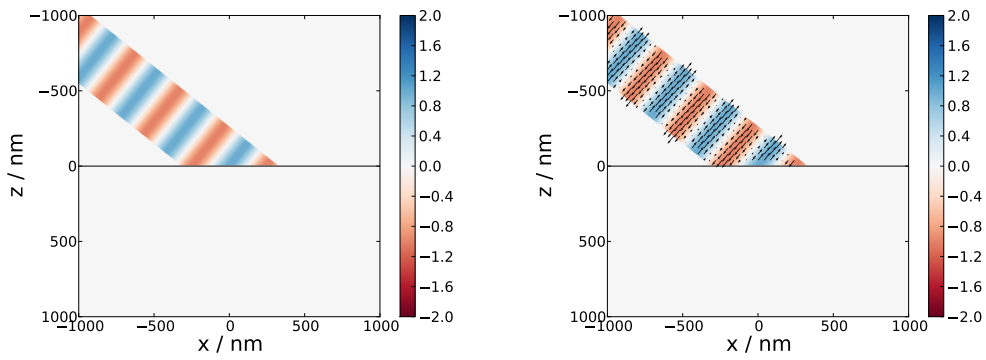
(a)
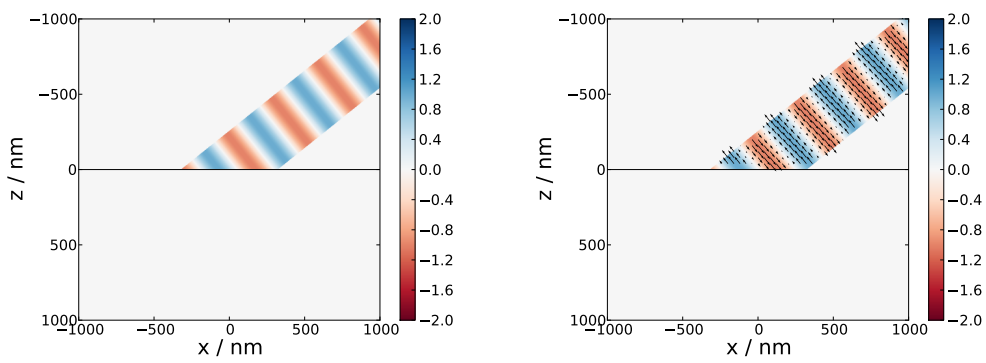
(b)

(c)

Figure 1: Caption over page. . . .

4

Figure 1: Electric field vector for (a) incident wave, (b) reflected wave and (c) all waves, including the evanescent wave below the interface. The left-hand side shows light polarised perpendicular to the plane of incident (the electric field vector coming into/out of the page); the right-hand side shows light polarised parallel to the plane of incidence (in this case the vector is shown as an arrow). The shading indicates the magnitude of the field, with the colour indicating the direction along the y-axis (left-hand column) or z-axis (right-hand column). The calculation is for 532 nm light with the incident medium having a refractive index of 1.4, the second medium having a refractive index of 1.0, and an incident angle of 51.3°. Diffraction at the edge of the plane wave and the Goos-Hänchen shift are neglected. The supplementary material includes two videos, depicting the two graphs of part (c) changing with time.

In total internal reflection spectroscopy, the probe light still has to pass through the higher refractive index medium and so it is important that this medium is clear in the region of spectroscopic interest. The probe light also samples an appreciable depth of the lower refractive index medium (typically around 100 nm–1 μm), while the width of the interface itself is often of molecular dimensions (one to a few nm); TIR methods lack the intrinsic surface sensitivity of non-linear optical methods. Whether the finite penetration depth of the evanescent wave is a disadvantage depends on the application and on the relative density of the molecules of interest at the interface compared to the thin layer of bulk that is probed.

There are a number of reasons for using TIR spectroscopy in preference to transmission spectroscopy. The most important is the confinement of the electric field close to the interface, giving surface sensitivity in the less optically dense medium. The second is an approximately two-fold enhancement of the electric field at the interface due to the overlap of the incident and reflected waves, leading to an increase in sensitivity. This effect is useful even when the surface sensitivity is not necessary, for example in sum-frequency generation where the surface sensitivity is intrinsic to the technique but a TIR geometry is still convenient experimentally since the signal scales as the sixth power of the electric fields at the interface. Finally, TIR techniques are useful when experimental considerations prohibit transmission spectroscopy, for example with opaque samples or with small volumes of samples such as proteins. The effective path-length can be controlled by selecting the number of reflections of the TIR beam. In such cases, surface sensitivity is not desired—and may be a problem if the surface region is significantly different from the bulk—and TIR simply offers a convenient way to probe a small depth of sample.

There are two main types of TIR spectroscopy: those that measure absorption of light by the sample, and those that measure emission or scattering of light from the sample. The first group are typically referred to as attenuated total reflectance (ATR) spectroscopies—to describe the fact that the intensity of reflected light is reduced, or attenuated, in the sample—and is most common with infrared light, although UV or visible light can also be used. In the second group the absorption of light is insignificant (although not actually zero, since some of the incident light is scattered or absorbed then re-emitted for the process to work) and the spectrum is contained in light emerging from the sample at a different wavelength. The two most common examples of this type of spectroscopy are total internal reflection fluorescence (TIRF) and total internal reflection Raman (TIRR).

This review is structured as follows. First, we discuss the optical theory of total internal reflection. Second, we describe typical experimental set-ups for the main variants of TIR spectroscopy, as well as briefly mentioning a few of the other uses of TIR illumination in spectroscopy that fall outside of the scope of this review. Third, we describe a range of applications for TIR spectroscopy in soft matter. We have selected applications that are either common-place or are novel and worthy of greater application. Where possible, we compare the relative merits of different techniques for each application.

2   Optical theory

Although the ATR techniques were developed before evanescent wave scattering—probably due to the ubiquity of infrared spectroscopy in chemical analysis—the scattering/emission techniques are easier to understand since the reduction in intensity due to absorption need not be accounted for. Additionally, as will be shown later in this section, the ATR techniques generate a number of experimental artefacts, primarily due to their use of a range of incident wavelengths. Therefore we will ignore the effect of absorption of light initially, and consider it later in this section.

2.1   Fresnel equations

The reflection and transmission of light at interfaces is governed by the Fresnel equations. The form of these equations for the case of total internal reflection is well known, but is worth repeating here since TIR spectroscopy is entirely dependent on these equations. In this section we only deal with non-absorbing media (where the refractive indices are real); in general, a

complex refractive index may simply be substituted into the equations given here to describe an absorbing material.

When light passes from one substance (with refractive index n_i) to another (with refractive index n_t), some of the light is transmitted, while some is reflected. The relative amounts depend on the polarisation of the incident light: either perpendicular to the plane of incidence (S), or parallel to the plane of incidence (P). (The incident and reflected beams and the surface normal all lie in the plane of incidence.) The reflection coefficient, defined as the ratio of the electric field of the reflected light to the electric field of the incident light, is

$$
\begin{aligned}
r_S &= -\frac{\sin(\theta_i - \theta_t)}{\sin(\theta_i + \theta_t)}\,, \\
r_P &= \frac{\tan(\theta_i - \theta_t)}{\tan(\theta_i + \theta_t)}\,.
\end{aligned}
\tag{1}
$$

The transmission coefficient, defined as the ratio of the electric field of the transmitted light to that of the incident light, is

$$
\begin{aligned}
t_S &= \frac{2\sin\theta_t \cos\theta_i}{\sin(\theta_i + \theta_t)}\,, \\
t_P &= \frac{2\sin\theta_t \cos\theta_i}{\sin(\theta_i + \theta_t)\cos(\theta_i - \theta_t)}\,.
\end{aligned}
\tag{2}
$$

In all the above equations θ_i is the angle between the incident beam and the surface normal and θ_t is the corresponding angle of the transmitted beam.

The angle of the transmitted light is given by Snell's law:

$$
n_t \sin\theta_t = n_i \sin\theta_i\,,
\tag{3}
$$

When $n_i > n_t$, θ_t is real only when θ_i is less than a critical angle,

$$
\theta_c = \arcsin n_t/n_i\,,
\tag{4}
$$

For a non-absorbing medium (which is usually the case in TIRR and TIRF), there is no net transmission of energy across the interface above the critical angle, however the boundary conditions still require there to be an electric field beyond the interface. This electric field is termed an evanescent wave, and decays exponentially with increased distance, z, from the interface.

$$
\mathbf{E}_t = \mathbf{E}_{0t}e^{-i(k_i x \sin\theta_i - \omega t)}e^{-k_t \beta z}\,,
\tag{5}
$$

where $\mathbf{E}_{0t}$ is the electric field of the transmitted light at the interface, $k_t = 2\pi n_t/\lambda_0$ is the wavevector of the transmitted light, k_i the wavevector of the

incident light, $\omega = 2\pi\nu$ is the angular frequency, and

$$\beta = \sqrt{\left(\frac{n_i}{n_t}\right)^2 \sin^2\theta_i - 1}\,. \tag{6}$$

The electric field decays with a characteristic length of

$$d_p = (k_t\beta)^{-1}\,. \tag{7}$$

Figure 3 (later in this section) shows the penetration depth with respect to angle of incidence for the silica–water interface. The decay length becomes infinite at the critical angle for a non-absorbing transmission medium: otherwise the light is attenuated by absorption and the decay length remains finite. Infrared absorption, Raman scattering and fluorescence are all linear spectroscopies: the signal is proportional to the intensity of the light and thus to the electric field squared, which drops off with distance twice as fast as the electric field. Consequently, TIR spectroscopies probe an interfacial region with a characteristic thickness of $(k_t\beta)^{-1}/2$. The variation of $\mathbf{E}_t$ with time and the position along the x axis is not particularly important for TIR spectroscopy, since the signal depends on the time-averaged field over the irradiated area.

Above the critical angle the transmission coefficients (also known as the Fresnel coefficients) are complex quantities given explicitly by,

$$t_{\mathrm{P}x} = \cos\theta_i(1 - r_{\mathrm{P}}) = \frac{2\cos\theta_i(\sin^2\theta_i - n_{ti}^2) + 2in_{ti}^2\cos^2\theta_i\sqrt{\sin^2\theta_i - n_{ti}^2}}{n^4\cos^2\theta_i + \sin^2\theta_i - n_{ti}^2}\,,$$

$$t_{\mathrm{S}y} = 1 + r_S = \frac{2\cos^2\theta_i - 2i\cos\theta_i\sqrt{\sin^2\theta_i - n_{ti}^2}}{1 - n_{ti}^2}\,,$$

$$t_{\mathrm{P}z} = n_{ti}^2\sin\theta_i(1 + r_{\mathrm{P}}) = \frac{2n_{ti}^2\cos^2\theta_i\sin\theta_i - 2i\cos\theta_i\sin\theta_i\sqrt{\sin^2\theta_i - n_{ti}^2}}{n_{ti}^4\cos^2\theta_i + \sin^2\theta_i - n_{ti}^2}\,. \tag{8}$$

where $n_{ti} = n_t/n_i$. The absolute values of the transmission coefficients are given in figure 2 for the case of a silica–water interface. The decomposition of the transmission coefficients into real and imaginary components (equation 8) is only useful for non-absorbing media, when n_{ti} is real. At the critical angle, $|t_{\mathrm{S}y}|$ and $|t_{\mathrm{P}z}|$ are both maximised with $|t_{\mathrm{S}y}| = 2$ and $|t_{\mathrm{P}z}| = 2/n_{ti}$. $|t_{\mathrm{P}x}|$ vanishes at the critical angle, but reappears above it. Therefore, scattering arising from only z-polarised incident light can be isolated at the critical angle.

A thin film at the surface with refractive index $n' \neq n_t$ modifies the equations for the Fresnel coefficients. If the film is thin compared to the
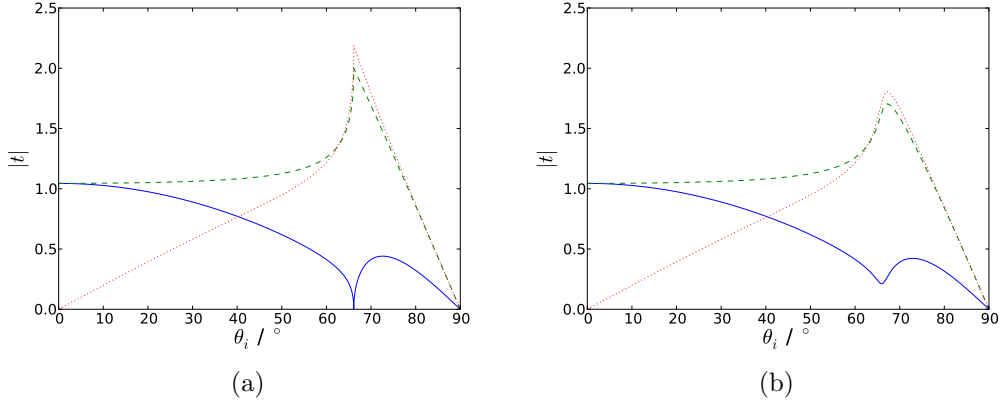
Figure 2: (a) Fresnel coefficients for the silica–water interface ($n_i = 1.461$, $n_r = 1.336$); (b) as part (a), but with n_t having an imaginary component of its refractive index of 0.01. The (real) refractive indices match fused silica and water at $532\,\text{nm}$. Solid blue line: $t_{\text{P}x}$; dashed green line: $t_{\text{S}y}$; dotted red line: $t_{\text{P}z}$.

wavelength of light, reflection and refraction within the film can be neglected and the electric fields in the film obtained from the continuity conditions at the interface. The z-polarised electric field within the film, $E_{\text{P}z}$, is thus multiplied by $(n_t/n')^2$;[†] $E_{\text{P}x}$ and $E_{\text{S}y}$ are unchanged.[4] Except for the cases of two thick materials in contact or two thick materials separated by a thin film, determination of the electric fields requires a matrix approach.[5]

2.2   ATR and effective penetration depth

For TIRR and TIRF the amount of light absorbed or scattered by the sample is a negligible fraction of the incident light. The refractive index of the transmitted medium is usually real and the formalism in section 2.1 applies.[6] ATR-IR, however, relies on absorption of IR light by the sample; absorption, in turn, depends on the imaginary part, κ, of the complex refractive index:

$$\hat{n} = n + i\kappa. \tag{9}$$

with κ, the [Note that an alternative definition for κ, $\hat{n} = n(1 + i\kappa)$, is sometimes used; in this paper we always use the version in equation 9]. For an absorbing sample $k_t\beta$ is no longer purely real (both k_t and β contain

---

[†]There is a typographial error in ref. 3 where the multiplication factor is stated as $(n_i/n')^2$
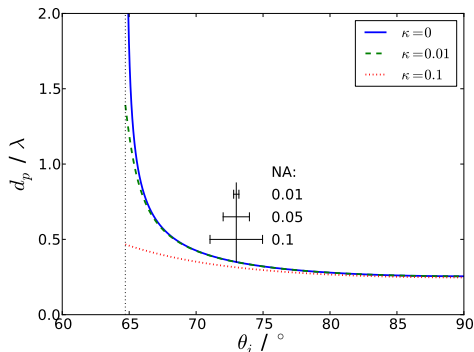
Figure 3: Penetration depth of the electric field at the silica–water interface ($n_i = 1.461$, $n_t = 1.336$) with respect to angle of incidence for a variety of different extinction coefficients. $\kappa = 0.001$ is indistinguishable from $\kappa = 0$ on this graph. The black horizontal bars show the spread of angles associated with different numerical apertures (NAs) of focusing lens.

imaginary parts) meaning that the light propagates into the sample (i.e. there is a net transfer of energy across the interface).[7] In this case, the penetration depth is obtained from the real component of $k_t \beta$. Figure 3 shows the penetration depth below a silica–water interface for a variety of different values of κ.

For ATR spectroscopy, equations 8 are important in that they determine the strength of the electric field in the sample and the absorbed energy is proportional to the square of the electric field. However, the value actually measured is the reflectance of the surface, $R = r^* r$, and therefore it makes more sense to calculate the reflectance term, rather than the magnitude of the evanescent field. Although the reflection coefficient is completely defined by equations 1 using an appropriate complex refractive index, it is not a particularly intuitive representation in that it does not directly relate the observed reflectivity to the concentration of a species in the sample. A common concept in ATR spectroscopy is to define an effective depth, d_{eff}, by analogy with the cell thickness, L, in the Beer-Lambert law

$$A = \log_{10} \frac{I_0}{I} = L \varepsilon c \tag{10}$$

where A is the absorbance, ε the extinction coefficient and c the concentration of the sample. So, for ATR spectroscopy,

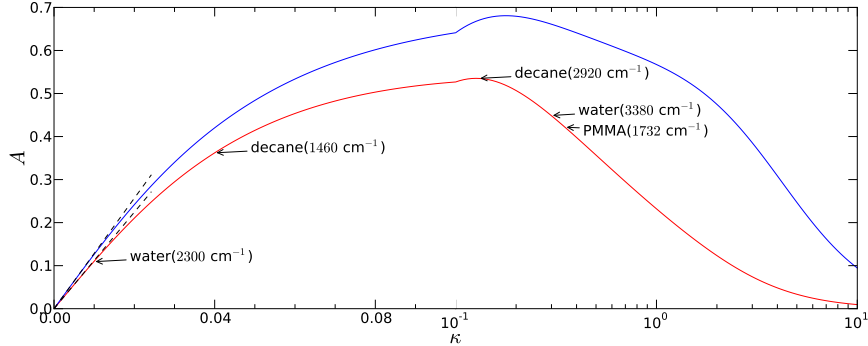$$A = -\log_{10} R = d_{\text{eff}} \varepsilon c \tag{11}$$

10

Figure 4: Absorbance ($A = -\log_{10} R$) at an interface with $n_i = 1.45$, $n_r = 1.35 + i\kappa$ and $\theta_i = 75°$ for S (red line) and P (blue line) polarisations. Absorbances approximated by the effective penetration depth model (equation 13) are shown as dashed lines. The graph also shows approximate absorbances for a variety of illustrative substances (values taken from refs. 9–11; the real part of n_r is not an exact match for these substances). Note the change from a linear to a logarithmic κ-axis half-way across the graph.

An expression for d_{eff} can be obtained from a Taylor expansion of R with respect to κ, retaining only the linear term.[8] The molar extinction coefficient ε is conventionally related to κ by

$$\varepsilon c = \frac{4\pi\kappa}{\lambda \ln 10} . \tag{12}$$

This Taylor series approach neglects the concentration dependence of the real part of the refractive index[7] and assumes ε is independent of c (i.e. $\kappa \propto c$).

Harrick proposed two limiting cases for the effective depth: the thick sample and the thin film.[12] These two cases are the same as those where useful approximations exist for the Fresnel coefficients (see equation 8 and adjacent text); for more complicated situations it is more practical to solve the Fresnel equations exactly rather than attempting approximations based on effective depth. In the thick sample limit, the extent of the sample is much larger than the d_p, and so the sample can be assumed to be homogeneous over the entire evanescent wave. Then

$$d_{\text{eff}} = \frac{n_t |t|^2 d_p}{2n_i \cos\theta_i} . \tag{13}$$

Note that d_p here is calculated for a non-absorbing sample, which is an appropriate approximation since linearising the expression for R is only valid
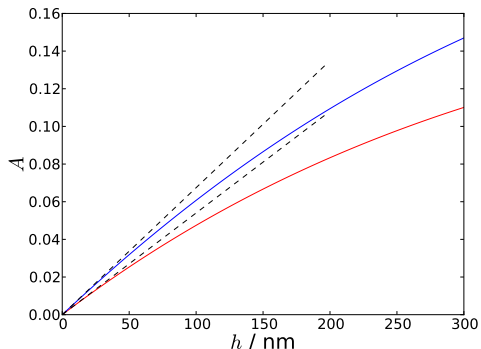
11

Figure 5: Absorbance ($A = -\log_{10} R$) at a three-layered interface as a function of film thickness with $n_i = 1.7$, $n_t = 1.35$, $n' = 1.4 + 0.13i$ (approximately equal to the CH stretch of decane[11]), $\nu = 2920\,\mathrm{cm}^{-1}$ and $\theta_i = 75°$ for S (red line) and P (blue line) polarisations. For comparison, absorbances calculated using the thin-film approximation (equation 14) are shown as dashed lines.

for weakly absorbing samples in any case. Figure 4 compares the absorbance obtained using equations 11 and 13 to the exact solution of the Fresnel equations. Absorbances from typical samples encountered in the spectroscopy of soft matter are also illustrated on figure 4. For the majority of pure substances, the main infrared peaks will be too strong for the linear approximations to absorbance to be valid. At high dilutions in a non-absorbing solvent, the linear approximation is valid.

In the thin film limit, the absorbing film is assumed to have a thickness, $d \ll d_p$, and hence the electric field over the film is constant. In this case

$$d_{\mathrm{eff}} = \frac{(n'/n_i)|t|^2 d}{\cos \theta_i} \, . \tag{14}$$

In both cases, t comes from equations 8, and hence the effective thickness depends on the incident polarisation. This dependence has important consequences when considering ratios of the different polarisations; ref. 13 contains a thorough discussion. The concept of effective penetration depth works better in the thin film approximation than in the thick sample approximation, especially for monolayers and bilayers of adsorbed materials, where the total amount of material present per unit area of the surface is very small. Figure 5 illustrates the applicability of thin film approximation to films of varying thickness, showing that the initial agreement is very satisfactory. For non-conducting films less than 10 nm thick, the thin film approximation is extremely good throughout the mid-IR.

12

For an ATR crystal with N reflections, the total reflectance is[13,14]

$$R = (1 - \varepsilon c d_{\text{eff}})^N \approx e^{-N\varepsilon c d_{\text{eff}}} \approx 1 - N\varepsilon c d_{\text{eff}} \, . \tag{15}$$

These approximate relations are only valid when $\varepsilon c d_{\text{eff}} \ll 1$.

2.3   Effect of ATR on band shape and position

For reasons explained in this section, ATR and transmission IR spectra of the same sample often appear different. Hence, one should be wary about assigning too much importance to small shifts in band position between ATR and transmission spectra or even to shifts in band position with a change in concentration. A number of methods have been developed to extract $\kappa(\nu)$ from an ATR spectrum as it is the absorption coefficient that is most relevant for the interpretation of spectra – such approaches are especially important for strongly absorbing samples or when working close to the critical angle. It is worth noting that ATR-IR is not unique in introducing distortions in the peak shape: all measurement techniques do so to some extent,[15] (including transmission spectroscopy, due to reflection losses on entering and exiting the sample), however the distortions arising from ATR-IR are particularly pronounced.

There are two main effects in ATR spectroscopy that distort spectra. The first arises from the linear dependence of the penetration depth and hence the effective path length, d_{eff}, on wavelength (equation 7). While this wavelength dependence causes small peak shifts,[12] its main effect is to change the relative peak heights in different parts of the spectrum. This effect only applies to thick films; for thin films the effective penetration depth is determined by the thickness of the film rather than the penetration depth of the evanescent wave. (Note that the correction for the wavelength dependence of d_p may be performed automatically by spectrometer software, and needs to be avoided for thin films).

The second effect is due to the variation of the real part of the refractive index near an absorption band. Based on equations 6 and 7, the depth sampled by the evanescent wave depends strongly on the refractive index of the sample. However, the real part of the refractive index of a substance changes sharply near its absorption bands, due to the requirement that the complex refractive index fulfils the Kramers–Kronig relationship (an equation arising from causality that relates the conservative and dissipative elements of physical phenomena).[16] A commonly used model to fit a vibrational absorption band is an antisymmetric linear combination of Lorentzian functions[17,18]

$$\kappa(\nu) = \frac{k_{\max}(\gamma/2)^2}{(\nu - \nu_0)^2 + (\gamma/2)^2} - \frac{k_{\max}(\gamma/2)^2}{(\nu + \nu_0)^2 + (\gamma/2)^2} \tag{16}$$
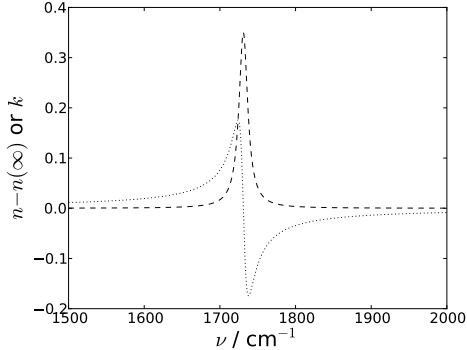
Figure 6: Variation in the real (n, dotted line) and imaginary (κ, dashed line) components of the refractive index for an absorption band with $k_{\mathrm{max}} = 0.35$, $\gamma = 15\,\mathrm{cm}^{-1}$, and $\nu_0 = 1732\,\mathrm{cm}^{-1}$. These parameters are chosen to be an approximate match for the carbonyl stretching band of the polymer PMMA (poly(methyl methacrylate)).[10]

where k_{max} is related to the oscillator strength of the vibrational transition, γ is the bandwidth at half-height and ν_0 the wavenumber at maximum intensity. The real part of the refractive index is then given by

$$n(\nu) \quad = \quad n(\infty) \;-\; k_{\mathrm{max}} \left[\frac{(\nu - \nu_0)(\gamma/2)}{(\nu - \nu_0)^2 + (\gamma/2)^2} - \frac{(\nu + \nu_0)(\gamma/2)}{(\nu + \nu_0)^2 + (\gamma/2)^2} \right] \quad (17)$$

(Typically $\gamma \ll \nu_0$ and hence the second term of equation 16 can be neglected near ν_0, although both terms are needed for the transformation to equation 17.) Figure 6 illustrates the form of n and κ near a vibrational transition. Figure 7 compares ATR and transmission spectra for the carbonyl stretch in PMMA for two polarisations and two angles of incidence. The consequence of the strong variation in refractive index in the vicinity of ν_0 is a shift in the absorbance maximum in ATR spectra towards lower wavenumber compared to transmission spectra. The variation of the refractive index affects both the penetration depth (which is not an issue in the thin-film approximation), and the amplitude of the electric field at the interface (eqn. 8, affecting both the thick- and thin-film approximations). Note that the peak shift is larger the closer one is to the critical angle. An additional complication illustrated by figure 7 is that the peak shift is not identical for the two incident polarisations, meaning that, at a fixed wavelength, the ratio of the two polarisations—often used for determining molecular orientation, see section 3.6—can change.

Where the complex refractive index is well known, it is relatively straight-
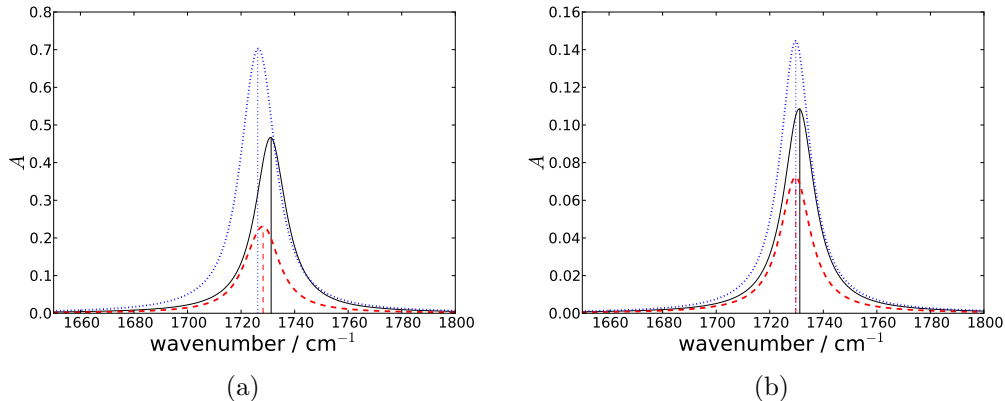
14

Figure 7: Comparison of simulated transmission IR (solid black line) and ATR-IR for S (dashed red line) and P (dotted blue line) polarisations. The transmission spectra were calculated from κ using equation 12, and have been rescaled to give a similar intensity to the ATR spectra. Peak maxima are labelled with vertical lines. (a) $\theta_i = 25°$; (b) $\theta_i = 45°$. The simulated spectrum is for the carbonyl stretch of PMMA (as shown in figure 6), with $n_{PMMA}(\infty) = 1.42$ and a germanium substrate $n_{Ge} = 4.0$. For these parameters, $\theta_c \approx 20°$.

forward to account for the peak-shift. However, where it is not well known—for example, peak-shifts caused by changes in chemical environment are frequently of interest—then it is more difficult to calculate the true IR spectrum from a measured ATR-IR spectrum.

Iterative methods have been proposed to extract the complex refractive index from an ATR spectrum.[17,19,20] The imaginary part of the refractive index (κ, the absorption coefficient) is estimated from the experimental spectrum; the real part of the refractive index, n, is calculated through the Kramers–Kronig transform of κ; n and κ are used in the Fresnel equations to reproduce a predicted spectrum, which is compared to the measured spectrum and then used to generate a better estimate for κ. The accuracy of algorithm depends on the quality of the method used to guess κ, the accuracy of the numerical Kramers–Kronig transform, and the accuracy of the Fresnel calculation (for example, does it describe a system with the correct number of layers?).

Where multiple absorption bands are next to each other—such that the adjacent bands fall within the modified refractive indices of each other—there is also a change in the relative heights of the bands. This effect is illustrated in the simulated spectrum containing two identical bands in figure 8. This
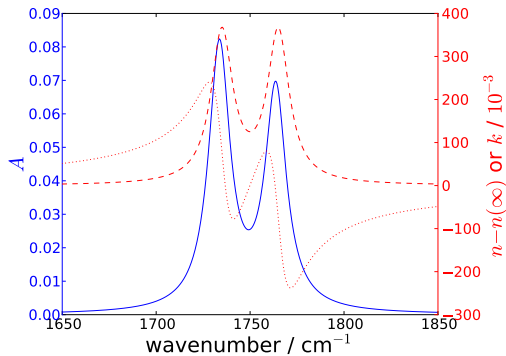
15

Figure 8: Simulated ATR spectra (blue solid line, left y-axis) of two identical absorption bands close to each other, illustrating the distortion in peak height due to the refractive index change associated with the absorption bands. $n_i = 4.0$, $n_t = 1.42$, $\theta_i = 45°$. n (red dotted line) and k (red dashed line)—both linked to the right y-axis—used to generate the absorption spectrum. The two bands have ν_0 of 1735 and 1765 cm^{-1}; otherwise the parameters are as in figure 6.

distortion is particularly insidious, since it might lead to a difference in concentration of two species being inferred when no difference actually exists.

2.4   Summary

For the three main spectroscopic techniques described here (ATR-IR, TIRR and TIRF) the signal is proportional to the squared electric field at the interface. For a single interface, the electric field is given by equation 8. The penetration depth into the second medium is given by equations 7 and 6. The special case of a thin film between two bulk substances is also readily described provided the film is thin enough that the electric field is approximately constant across it. For ATR techniques the absorption of light by the second medium must be accounted for. This correction is often made under the thin film assumption (equation 14) or is assumed to be proportional to concentration (equation 13), which is valid at low concentrations or for weakly absorbing media. ATR techniques cause the absorption bands to shift to lower wavenumbers, relative to maxima in the complex refractive index. For thin films or dilute samples this shift can be ignored but where it is important numerical methods exist to recover the complex refractive index from an ATR spectrum.

16

3 Experimental approaches

In this section we describe typical experimental arrangements for TIR spectroscopy. As before, we divide the techniques into two groups: the emission techniques, such as TIRF and TIRR, and the absorption techniques (ATR-IR, ATR-UV-visible and optical cavity techniques).

3.1 Emission spectroscopy

In TIR emission spectroscopy, a laser beam is totally internally reflected at an interface and the electric field of the evanescent wave excites the emission of light at a different wavelength from that of the laser. The primary experimental considerations are (i) delivery of the laser beam at a well-defined angle of incidence (so that the penetration depth of the evanescent wave is well defined), (ii) efficient collection of the emitted light (to maximise the signal), (iii) suppression of light emitted from regions other than the evanescent wave. The last consideration is probably the most important: signals arising from bulk samples tend to be much stronger than those from the thin evanescent region, especially for background fluorescence imposed over Raman spectra.

The excitation laser can be delivered either through the same objective lens used to collect the light or through a separate beam-path. In the former case, there are two main geometries employed, which are illustrated in Figure 9. One geometry (figure 9a) employs an off-axis Gaussian beam, beam focussed in the back focal plane of the objective.[21,22] This optical path produces light with a well-defined angle of incidence on the sample, but alignment can be difficult. A simpler approach is to use annular illumination[23] in which a ring of light is introduced into an objective with a high numerical aperture (NA), with a radius such that the light arrives at the sample above the critical angle (figure 9b). Annular illumination is not focussed at the back focal plane of the objective and so produces a wider range of angles of incidence at the sample. Additionally, the polarisation of the incident light is not preserved at the sample and even the overall light intensity at the sample forms a two lobed shape, and not a simple spot;[23] use of a radially polarised beam returns the shape of the probed volume to a spot[24] but does not allow the S and P polarisations to be independently probed. Objective-based illumination has a number of appealing features: it does not require significant modification to a standard fluorescence microscope, the objective provides good collection efficiency[25] and the tight focus of annular illumination avoids photobleaching outside the sample volume.[26] However, it also has a number of disadvantages: back-reflected excitation light, the possibility of
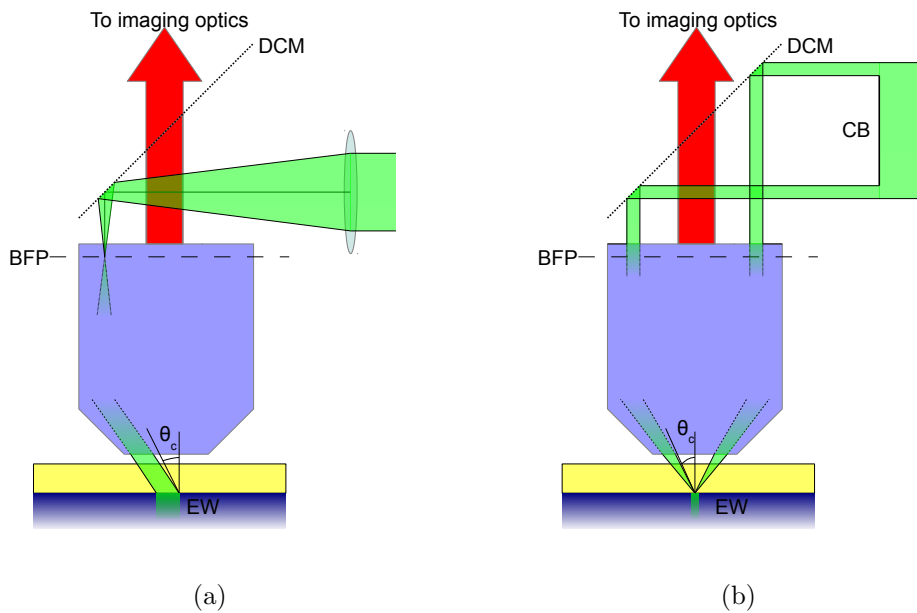
Figure 9: Schematic diagrams showing two means of achieving total internal reflection while illuminating through the collection objective (usually used in TIRF, but also applicable to TIRR). BFP (back focal plane), DCM (dichroic mirror), CB (circular block) EW (evanescent wave). The incident light is shown in green; the scattered/emitted light leaving the objective in red.
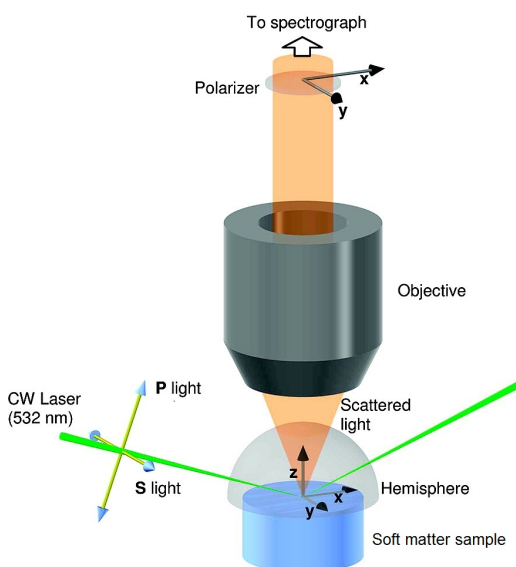
Figure 10: Optical arrangement for a TIR Raman spectrometer with a hemi-spherical substrate. The directions of the electric field vectors for the available polarisations of incident and collected light are also shown. Reprinted with permission from ref. 27. Copyright 2008 American Chemical Society.

fluorescence from optical elements in the objective or index-matching fluids, the cost and limited working depth of high NA objectives, sample damage from tightly focussed laser spots, and the limited damage threshold of the objective.[25]

The alternative mode of illumination is through a separate prism. This method provides fine control of the angle, spread and focus of the incident beam, beyond what can be achieved through the microscope objective. In our TIRR experiments, we focus the excitation laser at the centre of a hemispherical prism, which allows efficient collection of the emitted light and simple selection of the angle of incidence (there is no refraction on entry to the hemisphere since the light is always perpendicular to the curved surface). A half-wave plate selects the incident polarisation to be S or P. The emitted light is collected through the incident medium with a high NA ultra-long working distance objective. We direct the light into a commercial Raman spectrometer; for TIRF the light would typically be filtered by a dichroic mirror and imaged on a camera. The polarisation of the scattered light can be selected in either the x- or y-directions. Figure 10 illustrates this arrangement for our TIRR setup, but is also applicable to TIRF.

3.1.1 TIR-Raman

TIR Raman spectroscopy was first demonstrated practically by Ikeshoji and coworkers in 1973.[28] Early work used resonance-enhanced Raman to combat the weak signal from the sample and the strong signal from the substrate.[29–33] Iwamoto and coworkers[34,35] first demonstrated the utility of non-resonant TIR Raman when they recorded non-resonant spectra from a 1.1 μm polystyrene film mounted on a polyethylene substrate. Improvements in the performance of Raman spectrometers—together with judicious choice of substrates—now make TIR Raman spectroscopy feasible on very thin films (∼1–5% of a monolayer, equivalent to a 0.1 nm thick film) even with short exposure times (∼1 s). We have recently reviewed TIRR spectroscopy,[3] and a full description of the experimental set-up at Durham University can be found within 3, or in refs. 27,36. The majority of work on TIRR has been performed with separate illumination and collection optics. The alternative approach using annular illumination has only been used a few times.[37,38]

A major limitation of TIR Raman spectroscopy is fluorescence from the substrate, which can often dominate the Raman scattering from the evanescent wave. Many optical glasses (but not fused silica) are prone to fluorescence due to impurities in the glass, as is sapphire. Excitation in the red or near-IR reduces fluorescence, at the cost of reduced Raman signal (the Raman scattered intensity depends on ν^4, so the number of emitted photons, which determines the signal to noise, depends on ν^3) and, for near-IR lasers, reduced detector efficiency.

3.1.2 TIR-Fluorescence

Total internal reflection fluorescence was developed about five years after ATR-IR, and first used by Tweet *et al.* to study monolayers of chlorophyll at the water–air interface.[39] Hirschfeld then applied it at the solid–liquid interface[40] (although ref. 40 is hard to find). The development of through-objective illumination,[41] and subsequent refinements[21,42] are also significant in TIRF. The combination of TIRF illumination with fluorescence correlation spectroscopy and fluorescence recovery after photobleaching[43] was another step forward. TIRF is rarely used to obtain fluorescence spectra of the compounds present natively in the sample. Instead, fluorescently labelled probes are incorporated into the sample, with emission wavelengths chosen such that they can be separated by optical filters. This configuration is frequently used in imaging, and this represents an advantage of TIRF over the other techniques reviewed here, where imaging is more challenging. The high efficiency of fluorescence excitation means that single-molecule processes can readily

be followed, and millisecond time resolution is possible. Much of the work with TIRF microscopy relates to cell biology (reviewed in refs. 44–46).

Where detailed spectroscopic information is required from TIRF, commercial spectrofluorometers are readily adapted. For most applications one of the wide range of commercially available TIRF spectrofluorometer cells would be appropriate – however the literature provides examples of custom-built apparatus[47] including for specialised applications such as high pressures.[48]

The main developmental thrust in TIRF imaging in recent years has been to improve the lateral resolution below the 'diffraction limit' (which is typically around 300 nm). One method worthy of a brief introduction is two-photon fluorescence (TPF).[49] In TPF, the signal intensity depends on the square of the laser intensity, so the signal arises from a narrower region around the focus of a laser beam introduced through the objective.[23] The penetration depth probed is also halved compared to normal TIRF. (It should be noted, however, that if the same fluorescence transition is probed with one- and two-photon fluorescence, the lateral resolution and penetration depth are the same since the two-photon process uses double the wavelength). The improved lateral resolution must be obtained by scanning the beam across the sample (the shorter penetration depth applies with uniform illumination too). Finally, a sub-diffraction limit image can be built up over many frames by collecting fluorescence from single molecules and using centroiding approaches to determine their position.[50,51]

3.2 Absorption spectroscopies

In TIR absorption spectroscopy, the change in the intensity of the reflected beam with wavelength is measured. In comparison to emission techniques, TIR absorption spectroscopy suffers from the usual problem that it is much more difficult to measure small changes in large signal than it is to measure small signals against a null background. The ubiquity of infrared spectroscopy in the chemical sciences has, however, gone a long way to ensuring that good quality spectrometers are available for the task. The more general experimental challenge is to ensure that the reflected beam is collected from the sample with minimal—and above all, reproducible—losses. Stability is important since the background spectrum is rarely recorded simultaneously with the sample experiment and any small changes in the collection conditions can appear as strong features in the ratioed spectrum. Drift in the optical alignment and changes in the ambient atmosphere (especially CO_2 and water) must both be minimised.

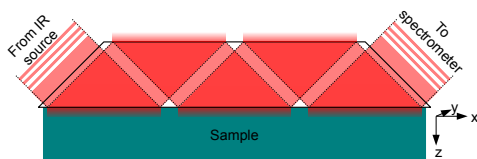ATR spectra are usually taken with a commercial spectrometer and com-

Figure 11: Schematic diagram of a typical ATR experiment using a trapezoidal ATR prism (applicable to both IR and UV-visible). The other shape for multiple-bounce ATR prisms is a parallelogram.

mercial ATR accessories are available for both infrared and UV-visible spectrometers. The internal reflection elements (IREs) are available both as single-bounce designs—for acquiring spectra of powdered samples without the need to make KBr pellets or disperse the powder in Nujol—and multi-bounce prisms which are more commonly used for soft matter applications.[52] One application where single-bounce ATR elements are required is in ATR-IR imaging,[53] discussed later in this review.

Figure 11 shows a typical ATR experimental arrangement. ATR prisms are available cut to a variety of different angles: 30°, 45° and 60° are fairly standard. The actual angle of incidence used can be varied, but it is most straightforward if it matches the angle of the prism. Distortions to the spectra are minimised the further the angle of incidence is above the critical angle, but with a concomitant loss of sensitivity due to unfavourable Fresnel coefficients. Total internal reflection takes place on both the upper and lower faces of the prism; in most experiments only one face is in contact with the sample, but the other face must be kept clean since spectra from this face will also be recorded. The entrance and exit faces of the prism are typically rectangular (longer in the y-direction than in the z direction (see figure 11 for axes). The beam is therefore usually focussed to an elliptical shape using curved mirrors before the prism. Figure 12 shows an arrangement for a single-bounce variable-angle ATR accessory (multiple-bounce accessories can be designed in a similar manner, although the foci of the incident and collection optics must be in separate places).

3.2.1 ATR-IR

ATR-IR spectroscopy was independently developed by Fahrenfort[55] and Harrick.[56,57] Early work explored different shapes of IRE and developed the theory of ATR spectroscopy including the modelling calculations surrounding the optical properties, of multi-layered systems and the approximations for
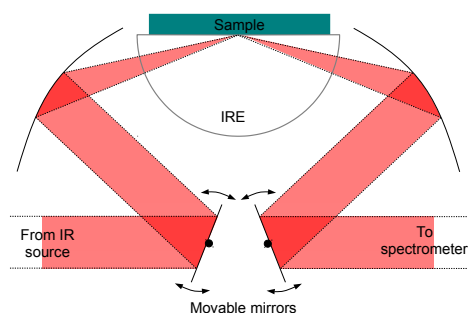
Figure 12: Schematic of a variable-angle ATR accessory, using movable mirrors to adjust the angle and fixed curved mirrors to focus the beam onto the sample. This is a simplified schematic based on the design in ref. 54.

the effective penetration depth. The classic book by Harrick,[12] reflects the emphasis of the early studies but remains useful today. The subsequent development of commercially available IREs and ATR accessories opened the technique up to a wider range of users and the application of the technique to an increasingly diverse range of samples.

3.2.2   ATR UV-visible

Although ATR UV-visible spectroscopy is experimentally straight-forward and operates on the same principles as ATR-IR, it has not seen significant use. One reason is that absorption cross-sections for strongly allowed electronic transitions (such as in dyes) are typically about 2–3 orders of magnitude higher than for vibrational transitions. Consequently, a monolayer of a chromophore on a surface may be detectable in a simple transmission experiment without the need for the signal enhancement arising from the ATR geometry. Nevertheless, the surface selectivity of the evanescent wave remains potentially beneficial in discriminating interfacial from bulk species. Conversely, molecules without aromatic or conjugated electronic structures often absorb very little light in the near-UV and visible regions, and so ATR-UV-visible spectroscopy is not a good tool for probing them. A second reason is that vibrational spectroscopy provides greater chemical selectivity and richer structural information then electronic spectroscopy, so ATR-IR is favoured. None-the-less, ATR accessories for UV-visible spectrometers are commercially available. The principal application of ATR UV-vis spectroscopy is to systems where a long path length is challenging, due either to high turbidity of a suspended catalyst,[58] or to strongly absorbing materials such as solvents

(in the UV)[59] or dyes.[60]

3.2.3 Cavity-enhanced techniques

An optical cavity around the sample serves to increase the path length within the sample through the use of multiple reflections. The key advantage of a cavity compared to a multiple reflection ATR crystal is that all the reflections in a cavity can occur at the same point. There are two basic experimental setups. First, the cavity is continuously illuminated by an incoherent broadband source, and the spectrum of intensity within is monitored using the small amount of light transmitted through the end mirror of the cavity.[61] This approach is known as cavity enhanced absorption spectroscopy (CEAS). Second, the cavity is illuminated with a short pulse of monochromatic light, and the decay of the pulse is measured from the light leaking through the end mirror (cavity ring-down spectroscopy, CRDS). CRDS is the more frequently used technique, but CEAS does have some advantages, including the use of broadband—and thus spectroscopically informative—light sources and the greater tolerance towards optical losses in the cavity.

Evanescent-wave cavity ring-down spectroscopy has recently been reviewed.[62,63] The basic experimental set-up consists of an optical cavity with highly reflective mirrors (reflectivity typically $> 99.9\%$) containing an IRE. A laser pulse is introduced into the cavity and the exponential decay of the intensity within the cavity is measured with and without the sample present. In the thick-film approximation (see section 2.2) the decay time is related to the absorption coefficient by[62]

$$\varepsilon C d_{\text{eff}} = \frac{nL}{\ln 10 \; c} \left[\frac{1}{\tau} - \frac{1}{\tau_0} \right] , \qquad (18)$$

where n is the average refractive index in the cavity, C the concentration of the analyte in the sample, L the length of the cavity, c the speed of light, and τ and τ_0 the characteristic $(1/e)$ decay time in the presence and absence of the analyte respectively. A big advantage of CRDS is that one measures the decay time of the pulse and not the intensity of the light, so the technique is insensitive to fluctuations in the laser power.[62] One of the main experimental challenges is to overcome the reflection losses at the entry and exit faces of the IRE. The most successful experimental design is the "folded-resonator", where the entry and exit faces of the IRE are reflectively coated and the only interface within the cavity is the one where total internal reflection takes place (figure 13). Alternatively a dove prism with anti-reflection coatings on the input and output faces can be used,[64] at the cost of reduced ring-down times due to reflection losses.
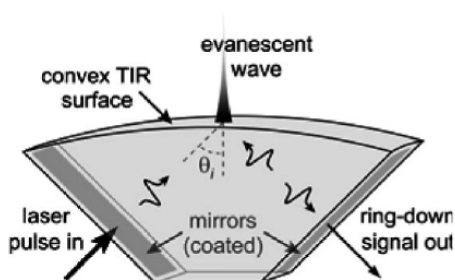
24

Figure 13: Schematic of a folded resonator cavity used in evanescent-wave cavity ring-down spectroscopy. Reprinted with permission from ref. 65. Copyright 2005 by the American Physical Society.

Evanescent-wave CDRS uses UV, visible and occasionally near-IR light sources. Although gas phase ring-down spectroscopy has used mid-IR sources,[66] to our knowledge these have not yet been used with evanescent waves. A few studies have used tunable lasers,[65] however the spectral range is small due to the limited bandwidth of highly reflective mirrors and the majority of work has used a single wavelength; consequently, the chemical discrimination of CRDS is currently limited.

3.3 Other techniques

3.3.1 X-ray techniques

For water (and most other substances) the refractive index in the X-ray region is less than unity and hence reflection from the air–water interface obeys the physics of total internal reflection (for this reason the phenomenon is also sometimes referred to as total *external* reflection or simply total reflection, to minimise confusion). Owing to the short wavelengths of X-rays, penetration depths are typically of the order of 10 nm.[67] X-rays eject core electrons from atoms and the resulting excited ion decays either by fluorescence or by the emission of a second valence electron (Auger process). The attenuation of the X-ray beam in total reflection X-ray spectroscopy is very slight and absorption is measured indirectly from X-ray fluorescence or the electron yield from photoelectrons, Auger electrons or other secondary electron processes.[68,69] In all cases, they are primarily atomic spectroscopies in that they provide information about the number of specific (usually heavy) atoms at the interface.[68]

The simplest X-ray technique is total reflection x-ray fluorescence, recently reviewed by Wobrauschek.[70] Here, the sample is illuminated by a

monochromatic X-ray source, and the emission spectrum (usually measured perpendicular to the surface) is recorded as a function of photon energy. The X-ray source can either be a synchrotron or an X-ray tube, allowing laboratory-scale experiments. Individual atomic transitions cause fluorescence at well-defined energies, and so the experiment provides an analysis of the elements present within the evanescent wave. As an example of an application relevant to soft matter, the influence of phospholipid monolayers on ion concentrations within an electric double layer has been determined.[71]

Greater information about the chemical environment of atoms at the interface is gained through use of X-ray absorption fine structure (XAFS). In these experiments, the energy of the incident X-ray is varied and absorption measured, typically using total X-ray fluorescence as a proxy for absorption.[72] XAFS spectroscopy requires intense X-ray sources and hence use of a synchrotron. Total reflection XAFS has been used to study adsorption at a variety of interfaces. For example, the presence of Br^- counterions for cationic surfactants has been measured at the water–air[69] and heptane–water[73,74] interfaces.

3.3.2 Non-linear spectroscopic techniques

Total internal reflection provides a convenient method of illumination for a variety of non-linear techniques. Second-order nonlinear optical techniques, such as sum-frequency generation (SFG) and second harmonic generation (SHG) are intrinsically surface sensitive[75,76] and TIR illumination is not required for surface selectivity at interfaces between centrosymmetric media. Nevertheless the enhanced electric fields at the interface from total internal reflection are useful.[77] A secondary benefit for infrared-visible SFG (a form of vibrational spectroscopy) is reduced heating due to the limited penetration depth of the IR laser into the sample. Third-order nonlinear optical techniques, such as coherent anti-Stokes Raman scattering (CARS) and stimulated Raman scattering are not intrinsically surface sensitive, but can be made so with TIR illumination (or with waveguide illumination, which is closely related).[78–80] However, these techniques require careful choice of the angle of the incident beams to satisfy the phase-matching requirements for the multi-photon process, a problem which is now almost invariably circumvented by the simpler technique of using a tight focus from a high numerical aperture objective.[81] Two-photon fluorescence, which is also a third-order nonlinear optical technique, has been used extensively as a variation of TIRF and is discussed elsewhere within the rest of this review.

26

3.4 Substrates and Samples

The refractive index is one of the main considerations when choosing a substrate for TIR spectroscopy. The ratio of the substrate and sample refractive indices determines the range of penetration depths available, with a larger ratio giving a smaller critical angle and the opportunity to use short penetration depths. This ratio is especially important for ATR spectroscopies since distortions in band shape are greatest close to the critical angle, and also because many multiple-bounce ATR elements are cut at 45° and so require a critical angle less than that value.

In all cases, the substrate should be clear in the spectral window of interest: since TIR spectroscopy is only surface selective with respect to the sample, any signal from the substrate will feature heavily in the spectrum. For emission spectroscopies such as TIR fluorescence and Raman there are two sides to this requirement. First, the material should be optically transparent at the wavelength of the probe laser (bearing in mind that small amounts of absorption can lead to heating and sample damage due to the high laser powers). Scattered light can be collected either through the substrate or the sample, so it is not essential for the substrate to be transparent to the scattered light. Second, the substrate should not have a strong spectrum in the same region as the sample. For Raman it is especially important that the substrate is not fluorescent since fluorescence cross-sections can be 13–14 orders of magnitude greater than Raman cross-sections,[‡] and so dominate the spectrum. Although it is possible to subtract the fluorescence signal from the Raman spectrum it is not possible to subtract the noise associated with the fluorescence signal. Fluorescence is reduced or eliminated at longer excitation wavelengths (in the red or near IR), although the Raman signal is also reduced (the number of Raman photons scales as ν^3). The sensitivity of TIRF to small amounts of fluorescence from the substrate depends on the number of photons expected from the sample.

Some of the most commonly used substrates for internal reflection spectroscopy are listed in table 1, together with approximate spectral windows. Most TIRF experiments are performed with silica windows, or simply through glass coverslips since they are transparent to visible light and do not fluoresce too strongly. For many ATR-IR experiments germanium is preferred, since it has one of the highest refractive indexes available and thus has a short penetration depth. ZnSe has a very wide spectral window, but is soft and

---

[‡]The fluorescence cross-section of the fluorescein dianion at 490 nm excitation is[82] 2.7×10^{-16} cm^2/molecule (from an absorption cross-section of 2.9×10^{-16} cm^2/molecule and quantum efficiency of 0.93). Raman cross-sections for comparison are given later in this review.

Substrate	Techniques	n (1064 nm)	Spectral window / cm^{-1}
Silica	Raman, fluorescence	1.45	50000–1600
Silicon	IR	3.56	8000–1500
ZnSe	IR	2.48	20000–650
Ge	IR	4.1	5500–830
Diamond	IR	2.39	30000–100 (small absorption bands from 4000–1400 nm)
Sapphire	IR, Raman	1.75	50000–1780 (IR) –800 (Raman)
CaF$_2$	IR, Raman	1.43	50000–1200

Table 1: Data for commonly used substrates in total internal reflection spectroscopy. This table is not intended to be complete, and the values given are approximate (for example refractive indices vary across the spectral window).

susceptible to scratching. Due to their high refractive indices, ZnSe, Ge and Si all suffer from significant reflection losses at the entrances and exits of the IRE. For IR and Raman spectra, crystalline compounds (such as sapphire or CaF$_2$) have sharper peaks than amorphous substrates and therefore suffer less from overlap with vibrational bands in the sample.

When the substrate of interest is not suitable for use as a prism in internal reflection spectroscopy, a number of options are available. Sometimes, it is possible to use a thin sheet of the substrate, index-matched to the main prism. An example is the use of mica in total internal fluorescence spectroscopy,[83,84] in which the mica is optically coupled to the glass coverslip with a liquid such as glycerol or a specialist optical adhesive. In other cases the film can be directly applied to the substrate, for example as a Langmuir-Blodgett deposited polymer layer,[85] a thin layer of ITO used to make an electrode,[86] or a thin coating of silicon on a ZnSe substrate[87] (to benefit from ZnSe's wider spectral window). Alternatively direct chemical modification of the surface is possible.[88–92] For mineral films it is often possible to use a micron-thickness film of solid particles. This approach has been used extensively for ATR-IR (ref. 93 provides an introduction to the topic), and has also seen limited use with TIR-Raman.[94] The particles themselves need not have a refractive index less that the supporting substrate, but instead the effective index of the particles and the surrounding solution should be less. In contrast to the planar surface it is impossible to know the exact region probed since this is a complex function of the scattering of the evanescent waves by the particles. A further restriction is the loss of polarisation information since molecules adsorbed to the particles are not oriented with respect to the plane

	Raman cross-section / $cm^2\,molecule^{-1}\,sr^{-1}$	IR cross-section / $cm^2\,molecule^{-1}$
water	4×10^{-30} (550 nm excitation) 4×10^{-28} (250 nm excitation)	1×10^{-18}
C–H	6×10^{-29} (532 nm excitation) # 5×10^{-27} (239 nm excitation)	3×10^{-19}

Table 2: Representative absorption/scattering cross-sections for Raman and IR spectroscopy. Raman cross-sections of water are for the $3400\,cm^{-1}$ band,[95]; Raman cross sections for the C–H stretch[96] are for cyclohexane between 2850–$2950\,cm^{-1}$; the IR cross-section of water[97] is measured at $3450\,cm^{-1}$; the IR cross section for the C–H stretch is for n-heptane[98] at $2900\,cm^{-1}$. Reproduced from ref. 3 (the value marked with # was mis-stated in this reference and has been corrected).

of the supporting substrate as they are with a planar surface.

The broad and strong IR bands of water cause a particular problem in ATR-IR. There are two important peaks: one between 2800–$3700\,cm^{-1}$ (O–H stretching) which obscures the C–H, N–H and O–H stretching bands of organic molecules and another around $1645\,cm^{-1}$ (H–O–H bend), which overlaps the amide I bands of proteins. In our recent review on TIR-Raman spectroscopy we compared the typical intensities of Raman and IR spectra of hydrocarbons and water in the C–H stretching region;[3] these are reproduced here in table 2. Although Raman has much smaller cross-sections overall, the C–H stretching cross section is approximately $10\times$ greater than the O–H stretch of water (excitation from visible light) whereas for infrared spectroscopy the C–H stretching bands have approximately $3\times$ lower cross-section than the O–H stretch of water. Therefore for aqueous samples, TIR-Raman may be a better choice than ATR-IR. In ATR-IR, the use of D_2O in place of H_2O can help to reduce the overlap between the water spectrum and the molecules of interest, but one has to be aware that the vibrational frequencies of exchangeable protons will shift to lower wavenumber when D replaces H. Aside from the spectral overlap, small changes in the amount of water within the evanescent field—for example if water is displaced by an adsorbate—can cause large changes in the background following subtraction of the reference spectrum from the sample spectrum.

A common problem with TIR spectroscopic techniques (especially TIRF) is light scattered into the sample by objects at the surface. This issue is especially prevalent for applications in cell biology. Two photon fluorescence is a common way to reduce surface scattering in TIRF.[25] In general, scattering

from inhomogeneous samples represents a limitation for TIR spectroscopy since it greatly reduces the precision with which the sample volume can be defined.

3.5   Calibration

In many applications of total internal reflection spectroscopy it is desirable to know the amount of material present, and thus to convert the measured signal—in either "counts" or absorbance—to a surface concentration. This section describes the calibration process.

Both TIR Raman and TIRF can be calibrated using the signal from the small amount of the chemical in the bulk. In our TIR Raman studies on surfactant adsorption we exploited the fact that for most surfactants the amount of surfactant adsorbed on the surface is constant at concentrations above the critical micelle concentration so all the change in the observed signal will be from the bulk. (Note that mixed surfactant systems can change above the cmc and so the calibration needs to be carried out independently on each pure component.) If the concentration is uniform with respect to distance from the surface, the signal above the cmc is a linear function of the bulk concentration:

$$
\begin{aligned}
S_{\text{total}} &= S_{\text{surface}} + S_{\text{bulk}} \\
&= [C_{\text{surface}}]Q + \int_0^\infty Q[C_{\text{bulk}}]e^{-2k\beta z}\,\mathrm{d}z \\
&= [C_{\text{surface}}]Q + \frac{Q[C_{\text{bulk}}]}{2k\beta}
\end{aligned}
\tag{19}
$$

where S is signal, $[C]$ concentration and Q is the calibration factor. This method relies on the additional assumptions that the spectrum from the bulk species is identical to that of the adsorbed species (which is true for disordered surfactant layers in our experience) and that the spread of the angle of incidence is small enough that its effect on β can be neglected. The latter assumption holds best far above θ_c. A number of different approaches have been used with TIRF, all of which rely on the assumption that the quantum yield of the fluorophore is not changed by adsorption.[99] The first approach is to scan variable depths of bulk sample, by changing the angle of incidence. At equilibrium the change in fluorescence signal should only arise from the change in Fresnel coefficients and the different depth of bulk solution probed. (This approach could also be applied in TIR-Raman, but to our knowledge has not been). The second approach uses a fluorescently labelled molecule that does not adsorb to the surface and which is injected in

increasing concentration during a separate experiment. Assuming that the fluorescence of the alternative molecule is identical to that of the molecule of interest—a reasonable assumption if the fluorophore is added as a label rather than being an intrinsic part of the target molecule—a linear calibration of signal against concentration can be obtained. Alternatively, where the adsorbate is irreversibly adsorbed, the bulk solution can be replaced with a label-free solution and the fluorescence intensity compared with and without the bulk contribution. It was realised quite early in the development of TIRF that the assumptions required for the calibration procedures above do not always hold: the fluorescence properties (quantum efficiency, lifetime and angular emission profile) can be perturbed by an interface, especially one with a metal film, and at high concentrations fluorescent molecules can self-quench removing the linear relationship between concentration and signal.[100]

The signal from ATR-IR is usually converted to surface excess using an extinction coefficient, ε, obtained through another method, often by coating the substrate with a known amount of sample or through transmission IR measurements. Using the thin-film model, and the assumption that the penetration depth and effective depth are both independent of concentration—which only applies for samples with a weak IR absorbance—a simple formula is obtained for the surface excess, Γ, analogous to the case of TIR-Raman:[101]

$$\Gamma = \frac{(A/N) - \varepsilon c_b d_{\mathrm{eff}}}{\varepsilon(2d_{\mathrm{eff}}/d_p)} \tag{20}$$

where N is the number of internal reflections and A is the absorbance of a relevant band.

3.6   Orientation and order parameters

The presence of a surface provides a reference plane for the orientation of nearby molecules. This orientation is often of interest since the mean orientation of adsorbed molecules gives an indication of the nature of the molecular interactions with the surface and the distribution of orientations indicates the degree of disorder.

The ratio of peak areas obtained with two incident polarisations can be used to determine the angle at which certain bonds are oriented towards the surface. For ATR-IR spectroscopy, the measured dichroic ratio, D, is calculated from the absorbances of S and P polarised light, A_{S} and A_{P} respectively,

$$D = \frac{A_{\mathrm{S}}(\theta_i)}{A_{\mathrm{P}}(\theta_i)} \tag{21}$$

(note that $1/D$ has also been used as a dichroic ratio). Using the effective penetration depth approximation,

$$D = \frac{d_{\text{eff,S}}\varepsilon_\text{S}c}{d_{\text{eff,P}}\varepsilon_\text{P}c} = \frac{|t^2_{\text{S}y}|\varepsilon_y}{|t^2_{\text{P}x}|\varepsilon_x + |t^2_{\text{P}z}|\varepsilon_z} \qquad (22)$$

where a subscripted value of ε represents the extinction coefficient for light with the electric field polarised in the subscripted direction. For an isotropic sample ($\varepsilon_x = \varepsilon_y = \varepsilon_z$) in the thick-film limit, $D = 0.5$ at $\theta_i = 45°$ (provided this is above the critical angle) – a convenient test for orientation since 45° is the most common angle in IREs. For the thin-film case, however, the value of D varies due to the $(n_t/n')^2$ term which is included in t_{Pz}. One difficulty that arises is that n' is not known *a priori* and cannot easily be measured for thin films. Further discussion of the interpretation of the dichroic ratio is given in ref. 13. Simplifications in the model—for example the neglect of oxide films on semiconductor IREs—can invalidate eqn. 22 so care must be exercised before using simplified expressions in place of the full Fresnel equations.

3.6.1 Molecular origin of the dichroic ratio

A fuller understanding of the origin of the dichroic ratio comes from consideration of the interaction of molecules with the incident electric field. In infrared spectroscopy the absorbance is related to the electric field by

$$A \propto (\mathbf{E} \cdot \mathbf{d})^2 \qquad (23)$$

where $\mathbf{d}$ is the transition dipole moment vector:

$$\mathbf{d} \propto \frac{\mathrm{d}\boldsymbol{\mu}}{\mathrm{d}q} \qquad (24)$$

where q is the vibrational coordinate and $\boldsymbol{\mu}$ is the molecular electric dipole. Therefore infrared absorption will be strongest when the transition dipole moment is aligned with the electric dipole of the infrared light. [A similar statement is also true of fluorescence, except that the change in state is electronic rather than vibrational.] Raman has slightly different rules: in Raman scattering the intensity of light emitted is given by $I \propto \mathbf{p} \cdot \mathbf{p}$ where $\mathbf{p}$ is the induced dipole of the molecule and is

$$\mathbf{p} = \boldsymbol{\alpha}_R(\nu) \cdot \mathbf{E} \qquad (25)$$

where $\boldsymbol{\alpha}_R(\nu)$ is the Raman polarisability tensor, which arises due to the change in molecular polarisability tensor over the course of a molecular vibration ($\mathrm{d}\boldsymbol{\alpha}/\mathrm{d}q$). [Note that in Raman (and fluorescence) spectroscopies
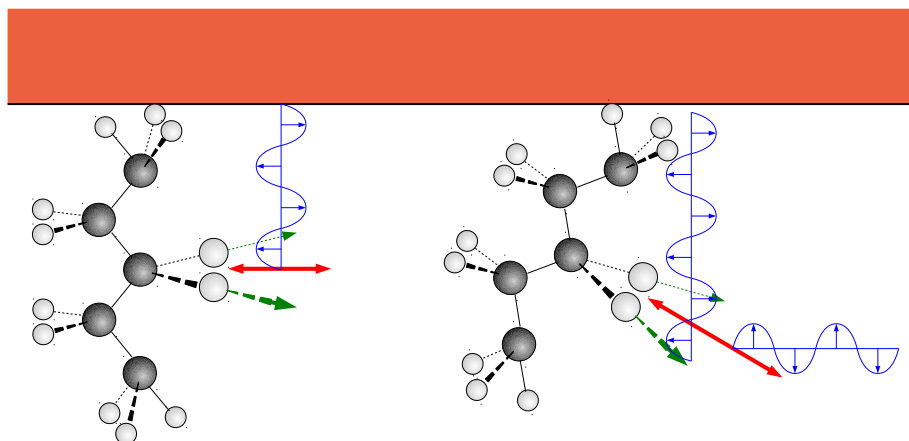
Figure 14: Schematic diagram illustrating the sensitivity of polarised spectroscopy to molecular orientation, using the symmetric methylene stretch as an example (the direction of the stretch is shown as green arrows). When the molecule is perpendicular to the surface the transition dipole moment (shown in red) is parallel to the surface, and may only interact with light polarised parallel to the surface; when the molecule is tilted the transition dipole moment may interact with both parallel and perpendicularly polarised light (both polarisations of light are shown in blue).

there is a second polarisation of interest: the emitted light also has a defined polarisation which is not necessarily the same as the incident light.] Raman scattering does not occur when the change in polarisability during a vibration is perpendicular to the electric field of the incident light.

Taking, for example, the case of a straight hydrocarbon chain oriented perpendicular to the probed surface, the CH_2 stretching vibrations cause a change in the dipole parallel to the surface. Therefore they are only excited by incident light parallel to the surface (exactly at the critical angle, by the S polarisation only). As the chain tilt increases, the CH_2 stretching vibrations are increasingly excited by light polarised perpendicular to the surface, and hence the measured ratio at the two incident polarisations will change. The case of the symmetric stretch is illustrated in figure 14. For Raman $d\boldsymbol{\alpha}/dq$ is greater along the bond than perpendicular to the bond, so similar arguments apply. However, the smaller contribution perpendicular to the bond cannot be ignored in quantitative work.

3.6.2 Order parameters

A straightforward and common means of interpreting the measured dichroic ratio is through the order parameter, S, defined following the standard definition used for liquid crystals[102]

$$S = \frac{3\langle\cos^2\theta\rangle - 1}{2}. \tag{26}$$

where $\langle\ldots\rangle$ denote an ensemble average and θ is the angle between the transition dipole moment and the surface normal. The order parameter is related to the measured dichroic ratio, D, by

$$\begin{aligned}
D &= \frac{|t_{Sy}^2|\langle\sin^2\theta\rangle}{|t_{Px}^2|\langle\sin^2\theta\rangle + |t_{Pz}^2|\langle\cos^2\theta\rangle} \\
&= \frac{|t_{Sy}^2|}{|t_{Px}^2| + |t_{Pz}^2|\left(\frac{2S+1}{2-2S}\right)}
\end{aligned} \tag{27}$$

It is important to note that θ is the orientation of the transition dipole moment which may not be along one of the principal axes of a molecule; determining a molecular orientation from that of transition dipole moment requires a coordinate transformation. More than one vibration is often required to determine a molecular orientation uniquely. For example, for a glycerophospholipid, the CH_2 symmetric and antisymmetric stretches and $C{=}O$ stretches are all polarised perpendicular to the hydrocarbon chain,[102,103] but there are multiple chain orientations that are consistent with a particular value of θ for any single mode. Dichroic ratios for two orthogonal modes (such as the carbonyl and CH_2 antisymmetric stretch) are required to determine the orientation of the chain. For proteins in a lipid membrane, the dichroic ratio for the amide I band is often used to obtain the angular distribution of α-helices. The experimentally determined tilt angle, θ, depends on an orientational average over three nested orientational distributions: the orientation of the membrane relative to the surface (θ_m), the orientation of the protein α-helices within the membrane (θ_α) and the orientation of the transition moment of the amide I band within the α-helices (θ_M).[104] θ_M is assumed to be a δ-function with a value of 39–40° while θ_m can be determined independently from the dichroic ratios of the lipid vibrations.[102]

To sound a further note of caution, the order parameter $\langle\cos^2\theta\rangle$ does not give an unambiguous distribution of angles, except at its two limits, $S = 1$ (transition dipole moment parallel to the substrate) and $S = -0.5$ (transition dipole moment perpendicular to the substrate). For example,[105] at $S = 0$ the distribution of chain angles could be completely isotropic, perfectly oriented

at the magic angle ($\cos^2 \theta = 1/3$) or an infinite number of distributions in between. To account for this ambiguity, some groups have described the orientational distribution using the maximum entropy method,[106,107] which obtains a model that provides the greatest possible multiplicity of states (i.e. the widest possible distribution of transition dipole moment angles) while still being consistent with the measured order parameters. Higher order terms, such as $\langle \cos^4 \theta \rangle$, can be obtained from TIRF[107] (and in principle also TIR-Raman) or by combining information from complementary techniques.[108]

4 Applications

4.1 Adsorption from solution

Both the equilibrium and time-dependent behaviour of molecules adsorbing to solid surfaces have been studied extensively by total internal reflection spectroscopic techniques. Within this review we focus particularly on mixed systems, since differentiation of components in a mixture is the key advantage of spectroscopic methods over alternative techniques such as ellipsometry or quartz crystal microbalance. The majority of this section concerns adsorption at the solid–liquid interface but we also briefly cover the liquid–liquid interface, which is much more challenging to study spectroscopically.

4.1.1 Isotherms

ATR-IR has been used extensively for studying adsorption at solid–liquid interfaces,[105,109,110] in particular for the adsorption of mixed systems.[111,112] For mixed surfactant systems, multiple components are typically distinguished by deuteration of the hydrocarbon chains, but this is not always necessary and the CH stretching bands around $2900\,\mathrm{cm}^{-1}$ can provide sufficient information on their own.[111,113] For example, the widely studied C_nTAB surfactants (a trimethylammonium bromide headgroup with various lengths of hydrocarbon chain) have a distinctive CH_3 stretching bands from the methyl groups on the trimethyl ammonium headgroup at $2985\,\mathrm{cm}^{-1}$ (symmetric stretch) and $3040\,\mathrm{cm}^{-1}$ (antisymmetric stretch). Neivandt *et al.* used this band to distinguish C_{16}TAB from the polymer poly(styrenesulfonate).[113] (They also used the UV absorption of the polymer with UV-ATR to provide a second method of quantifying the two components.) We recently looked at a mixture of the surfactants Triton X-100 and C_{16}TAB,[114] using their C–H stretching bands (discussed in section 4.1.2 below). Lower frequency bands from surfactant headgroups, such as S–O stretches in sulphate headgroups or N–C stretches in methyl ammonium headgroups, are often sensitive to environment so may
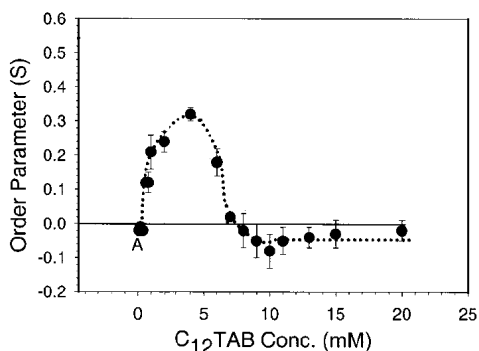
Figure 15: Order parameter (as defined in eqn. 26) of the surfactant C_{12}TAB adsorbed on silicon as a function of the bulk surfactant concentration. Reprinted with permission from ref. 102, and adapted. Copyright 2001 American Chemical Society.

provide useful information on packing and local ionic strength.[112,115] However, they are often obscured by bands from the substrate. An interesting application of ATR-IR involves the adsorption of chiral surfactants onto a chiral substrate.[90,116] The incoming flow of surfactant was repeatedly switched between two enantiomers and modulation spectroscopy[117] was used to resolve the very small differences between the spectra of the two adsorbed surfactants, arising from the chiral chemical environment on the surface.

TIR spectroscopy also provides information about the orientation of molecules at a surface (see section 3.6). The order parameter derived from the measured dichroic ratio in ATR-IR spectra is shown in Figure 15 for the adsorption of C_{12}TAB on silica.[118] The hydrocarbon chains showed no order at very low surface coverage, some preferred orientation of chains normal to the surface at intermediate concentrations and then no order again at higher coverages, probably reflecting a micellar structure where average chain orientation is isotropic.

4.1.2 Kinetics

Internal reflection spectroscopy has been used extensively to follow the kinetics of adsorption. Tabor *et al.* reported the adsorption of nonionic[110] and cationic[119] surfactants onto silica from toluene. The IRE was a multiple-bounce element, with a length of 80 mm, and data were recorded with a time resolution as fast as 4 seconds. Although internal reflection spectroscopy is most informative when looking at planar surfaces, adsorption onto particulate substrates such as alumina and TiO_2 has been widely studied[109,120,121]

(see the discussion of particulate substrates earlier in this review). One of the earliest examples was by Couzis and Gulari, on sodium laurate adsorption onto alumina.[121] The process was very slow (equilibrium was not reached in 25 hr) and so short acquisition times were not required. Inorganic ions, such as phosphate and sulphate, have characteristic vibrations that can be used to study adsorption kinetics.[120] TIRF has also been used to measure the kinetics of adsorption and desorption, primarily of proteins[122–125] but also of polymers.[126,127] In all cases the target molecule was fluorescently labelled. Fu and Santore used fluorescent labelling to distinguish between chemically identical polymers with different molecular weights[127]—something which would be almost impossible to do without labelling. TIRF is well established for studying protein adsorption, because fluorescent labelling of proteins is commonplace in molecular biology to distinguish different proteins. TIRF is less well used for polymers, since other non-invasive methods are often available (typically optical reflectometry), and almost never used for surfactants, where a fluorescent label would significantly change the properties of the surfactant.

Internal reflection spectroscopy has seen surprisingly little use for the measurement of adsorption kinetics of mixed systems. One elegant example is the work of Ducker and coworkers on the exchange kinetics in adsorbed films of tetradecyl trimethylammonium bromide[128] and didodecyldimethylammonium bromide.[129] The surfactants were replaced with their deuterated analogues allowing the incoming and outgoing surfactant to be identified, and the kinetics recorded with 2-s time resolution. Recently, we have used TIR-Raman to study the adsorption kinetics of both single component[36] and multicomponent surfactant systems.[114] Target factor analysis[130] (TFA)—a variation on principal component analysis—allowed the separation of the contributions from two overlapping surfactant peaks even from comparatively noisy kinetic spectra with a 1-s acquisition time. The methyl stretches of $C_{16}TAB$ (described above in section 4.1.1) and the aromatic C–H stretch of Triton X-100 (at $3080 \, cm^{-1}$), were the key differences between the hydrocarbon groups of the two surfactants. Figure 16 illustrates kinetics spectra and the resulting component weights; although methods such as TFA are outside the scope of the review, it is a useful reminder of the value of chemometric methods when processing TIR spectroscopic data. For adsorption from aqueous solutions, Raman spectroscopy offers a key advantage over infrared spectroscopy due to the comparative insensitivity of the spectra to the surrounding water. This increase in the ratio of signal to background allowed us to acquire spectra from only a single bounce of a loosely focussed ($\sim 30 \times 10 \, \mu m$) laser beam. For the measurement of adsorption kinetics—which are often governed by mass transport—it is much easier to control mass transport within a small region than over the whole of large ($\sim 5 \times 2 \, cm$) infrared IRE.
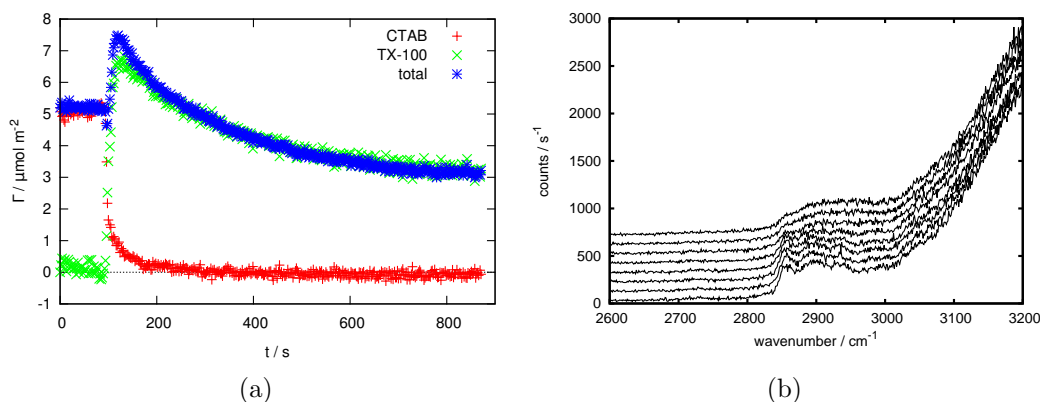
Figure 16: (a) Kinetics of replacement of the surfactant $C_{16}TAB$ with the surfactant Triton X-100 at the silica–water interface, measured by TIR Raman spectroscopy. (b) 10 sequential spectra of the CH stretching region representing $t = 89$–$105\,s$ of the processed data shown in part a, 1-s exposure time, S polarisation. The individual spectra illustrate the level of signal to noise and the similarity between the spectra of the two surfactants. The spectra are offset for clarity. Reprinted with permission from ref. 114. Copyright 2011 American Chemical Society.

TIRF provides two means to measure kinetics of adsorption even when the system is at equilibrium.[100] The first is to use correlation spectroscopy. Here, only a very small number of molecules ($\sim$100) are in the field-of-view at any one time,[131] by having a small surface coverage, a small sampling area, or by only fluorescently labelling a small fraction of the available adsorbates. The time autocorrelation function of the fluorescence intensity provides information on how long molecules stay within the evanescent wave. TIR-fluorescence correlation spectroscopy has been applied widely, for example to dyes at the solid–liquid interface,[132] the interaction of proteins and antibodies,[133] adsorption and binding to supported membranes,[131], the adsorption and desorption kinetics of different dendrimers[134] and the competitive adsorption of proteins and surfactants.[135] An alternative approach is fluorescence recovery after photobleaching (FRAP or FPR). Here, surface-bound molecules are made non-fluorescent by photobleaching and the time required for the fluorescence intensity to recover is measured. FRAP is also sensitive to lateral motion within the adsorbed layer, which is particularly relevant to biological membranes such as lipid bilayers,[136] proteins[100] and DNA fragments.[137] with either a confined detection volume[131] or imaging.[138,139]

Evanescent wave cavity ring-down spectroscopy has been used to ob-

tain adsorption isotherms for a range of substances including dyes[64] and proteins.[140] However, evanescent wave CRDS is particularly powerful when looking at adsorption kinetics. It has an inherently short acquisition time defined by the cavity ring-down time (in the microsecond regime), and so it is possible to acquire data quickly without the need for long integration times (though averaging multiple ring-downs does improve signal to noise). Examples include the adsorption kinetics of haemoglobin,[141] the dye Rhodamine B,[142] ruthenium complexes on polyelectrolyte films,[143] and protein adsorption on a non-stick polymer surface.[144] The last two examples show that evanescent wave CRDS spectroscopy is not restricted to the unfunctionalised surfaces of the TIR element.

4.1.3 Liquid–liquid interface

The liquid–liquid interface is particularly challenging to study by spectroscopic techniques since molecular liquids frequently have complex spectra that obscure the spectroscopic bands from molecules at the interface. The problem is particularly acute in vibrational spectroscopy where overtones and combination bands can fill much of the vibrational spectral window. With TIR Raman, all the studies to date have used resonance Raman to enhance the signal from the adsorbed molecule and have been limited to aromatic dyes. For example, Watarai and coworkers studied the adsorption of a manganese porphine complex to the toluene–water interface[145] and the aggregation of protonated tetraphenylprophyrin at the dodecane–water interface.[146] ATR-IR is even more challenging since the possibility of using resonances with electronic transitions does not exist. Sperline and Freiser used ATR-IR to study the adsorption of the surfactant cetyl pyridinium chloride at a hydrocarbon–water interface.[147] They used a thin ($\sim 1\,\mu$m) hydrocarbon film to minimise absorption of the infrared light within the film.

TIRF at the liquid–liquid interface is experimentally simpler since most solvents are not fluorescent, however it suffers from the usual limitation of requiring fluorescently labelled adsorbates. With pulsed lasers, the time-dependence of the fluorescence decay provides insight into dynamics at the liquid–liquid interface. For example, the form decay of the fluorescence anisotropy of the different collection polarisations reveals whether adsorbed molecules are able to rotate in three dimensions (indicating a rough interface) or only in the plane of the interface (indicating a smooth interface).[148] Tracking singly labelled molecules adsorbed alongside unlabelled molecules allows determination of both the adsorption kinetics (from the rate at which labelled molecules appear) and the aggregation state (larger aggregates diffuse more slowly in the plane of the interface).[149] More detail about techniques
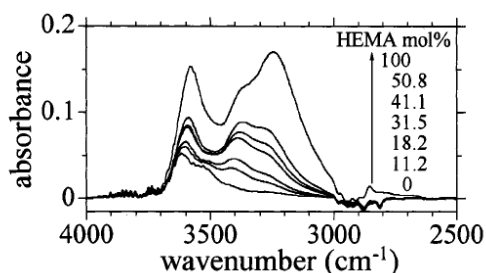
Figure 17: Change in the ATR-IR spectrum of water sorbed into a variety of PMEA and PHEMA copolymers. Reprinted with permission from ref. 156. Copyright 2003 American Chemical Society.

for the study of liquid–liquid interfaces (not restricted to TIR spectroscopy) can be found in references 150,151.

4.2   Polymers

Total internal reflection spectroscopy, primarily ATR-IR, has been used to study polymer structure and its response to external perturbations. Polymers can be readily cast onto an ATR crystal and the short path length in ATR-IR allows even opaque materials to be studied. Katsumoto *et al.* studied the polymer poly(N-isopropylacrylamide) during a temperature-induced transition from a coil to a globule conformation.[152] The amide I and II bands changed at different rates across the phase transition which they attributed to the amide I band responding mainly to the sudden breaking of hydrogen bonds at the transition, while the amide II band also responded to the slower change in chain conformation. The presence of an interface can change the properties of polymers. Depth profiling (see section 4.5) showed that the surface of PET has more trans conformers than the bulk material;[153] changes in orientation were harder to interpret quantitatively.[154] The influence of a manufacturing process on the orientation of a polymer is a topic of practical interest since many polymers are drawn as part of their manufacture. Chuah used the ATR-IR dichroic ratio to study the effect of drawing on the polymer PTT[155] and found that drawing did increase orientation, as expected.

ATR-IR spectroscopy provides a convenient way of studying diffusion into the thin slice of material within the evanescent wave (see review by Barbari and coworkers[157]). The diffusion of solvents within polymers is highly relevant to polymer processing but also to more diverse applications such as methanol fuel cells.[158] Yarwood and coworkers published an extensive body of work looking at the diffusion of water within polymers.[159–161] Polar organic

groups show clear spectral changes upon hydration, for example, in the S–O stretching region around $1080 \, \text{cm}^{-1}$,[159] and the O–H stretching band of the water at 3000–$3800 \, \text{cm}^{-1}$ is sensitive to the interaction with the polymer.[161] A recent example from the work of Ike *et al.* is displayed in Figure 17, which shows the incorporation of water into the polymers poly(2-methoxyethyl acrylate) (PMEA) and poly(2-hydroxyethyl methacrylate) (PHEMA) as well as their copolymers.[156] The shape of the water spectrum varied dramatically with polymer composition: the strong bands around 3200 and $3400 \, \text{cm}^{-1}$ were attributed to water hydrating the hydroxyl groups of PHEMA while the bands from 3500–$3600 \, \text{cm}^{-1}$ were assigned to water hydrating carbonyl or ether groups. Diffusion studies are not restricted to simple polymers, for example Döppers *et al.* used ATR-IR to study diffusion into polymer–clay nanocomposites.[162]

The diffusion of molecules through the skin is important for many drug delivery applications, and is often modelled using a polymer layer rather than a real biological sample. The model "skin" membrane is applied to the IRE, and the drug molecule injected into solution on the opposite side of the membrane. The passage of the drug molecule through the membrane is then monitored by ATR-IR. One experimental difficulty is ensuring effective contact of the membrane with the substrate.[163]

4.3   Biological soft matter

Total internal reflection spectroscopy has been used extensively to study biological systems. For the purposes of this review we will restrict discussion primarily to lipid membranes, proteins and their mixtures. However TIRF especially has been used extensively to study cells bound to surfaces; we provided some relevant references earlier in section 3.1.2.

4.3.1   Lipids

The TIR substrate provides a natural support for a planar supported lipid bilayer (PSLB). The formation of bilayers has been studied by a number of different methods. Lee and *et al.* used TIR Raman spectroscopy to follow the deposition of DPPC bilayers from mixed micelles of DPPC and β-D-dodecyl maltoside with $\sim$45 s time resolution.[164] A deuterated lipid was employed to separate the signals from the lipid and surfactant. The ratio of the intensities of the C-H and C-D stretches shows the initial adsorption of lipid-surfactant mixed micelles followed by the progressive replacement of surfactant by lipid. The conformational order of the lipid chains was inferred from the ratio of the antisymmetric and symmetric methylene stretching bands, which increased
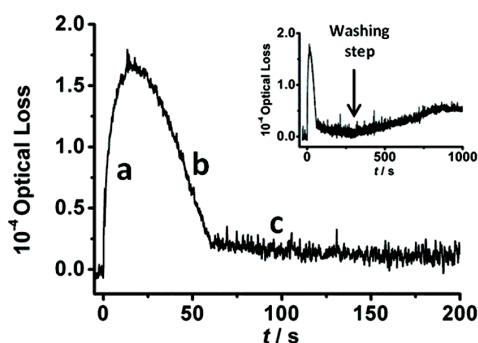
Figure 18: Formation of a lipid bilayer by vesicle fusion, studied by evanescent wave cavity ring down spectroscopy. a: adsorption of vesicles to the surface, b: fusion of vesicles and c: complete formation of a bilayer. The inset shows a longer timescale with rinsing starting at $300\,$s. The surface concentration at the peak is estimated to be $6.9 \times 6^{-10}\,\mathrm{mol\,m^{-2}}$. Reprinted with permission from ref. 166. Copyright 2012 American Chemical Society.

slightly during the deposition process showing the lipid chains were becoming more ordered. Bayerl and coworkers used ATR-IR to follow vesicle fusion of mixed cationic/zwitterionic lipids, showing a slow change in lipid composition as the fusion process progressed.[165] Very recently, Unwin and coworkers used evanescent wave cavity ring-down spectroscopy to follow the formation of lipid bilayers by vesicle fusion,[166] shown in figure 18. While CRDS has excellent time resolution, with a single wavelength of light in the cavity it is not possible to follow different components: for mixtures, Raman or IR spectroscopy are preferred. TIRF has also proved to be a powerful tool for investigating bilayer formation via vesicle fusion. For example, individual vesicles doped with a fluorescent protein can be seen sticking to the bilayer and not fusing—in which case the fluorescence intensity remains as a point source—or fusing into the bilayer—in which case the fluorescence spreads out as the protein diffuses within the bilayer.[167] Examples of the use of FRAP to study lateral motion in PSLBs are given earlier, in section 4.1.2.

Many lipid bilayers undergo temperature-dependent phase transitions. Lee and Bain used TIR Raman spectroscopy to characterise the phase transitions of a number of different PSLBs.[168] The ratio of the intensities of the C–H stretching modes in S and P polarised spectra is sensitive to chain tilt, while the ratio of the antisymmetric to the symmetric CH_2 stretching bands and the wavenumbers of these two bands provide an indication of chain ordering (the number of gauche defects).

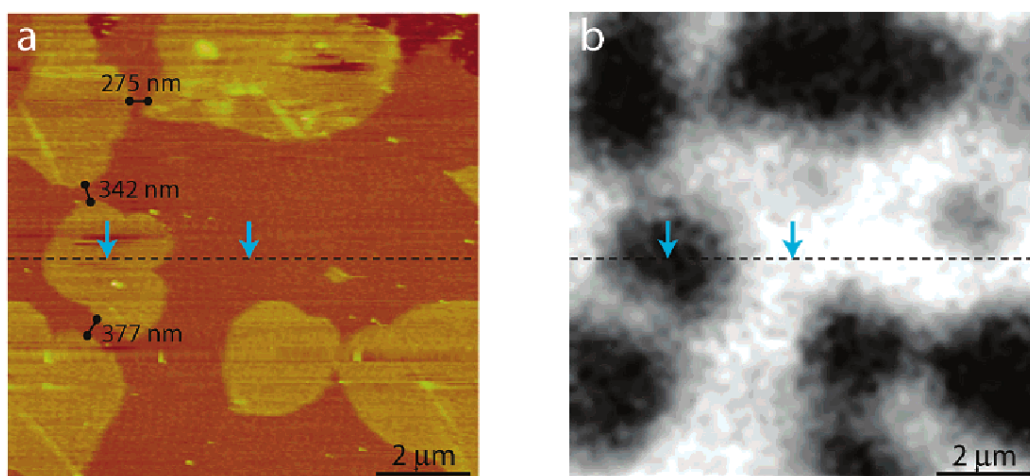Under certain conditions lipid bilayers can phase separate, forming do-

Figure 19: Imaging of lipid domains by tapping mode AFM (a) and TIRF (b). Although TIRF has lower resolution since it is diffraction limited, it is also able to acquire images more quickly (fractions of a second as opposed to minutes). Reprinted with permission from ref. 169. Copyright 2003 American Chemical Society.

mains with separate compositions and degrees of packing (this often happens in the presence of cholesterol, with the cholesterol preferentially occupying the "liquid-ordered" phases).[170] To study these bilayers an imaging technique is preferred, since a purely spectroscopic measurement either records the average spectrum of both domains or a random choice of a single domain depending on the area probed. Yip and coworkers studied these phase-separated domains with TIRF in combination with AFM,[84,169] allowing verification of the position of the domains through two independent methods (see figure 19). Typically the fluorescence signal comes from a fluorescently labelled lipid (or cholesterol) added in ~1% mole fractions. Polarised TIRF provides information about chain tilt in the different phases, on the assumption that the fluorescent probe does not perturb the local structure of the lipids.

4.3.2 Proteins

A number of reviews describe the general use of IR spectroscopy for the determination of secondary structure of proteins.[171–173] Most information comes from the amide I band around $1650\,\mathrm{cm}^{-1}$ (primarily a C=O) stretching vibration. The position of the band indicates the environment:[172] α-helices appear from 1648–$1660\,\mathrm{cm}^{-1}$, antiparallel β-sheets between 1675–$1695\,\mathrm{cm}^{-1}$, β-

sheets from 1625–1640 cm^{-1} and a disordered structure from 1640–1648 cm^{-1}. Since these bands are all close to each other and overlapping (the ranges above describe the peak position; the bandwidth is larger) and since most proteins contain more than one secondary structure, it is necessary to use either the second derivative or Fourier self-deconvolution to identify the peaks. Goormaghtigh and coworkers presented a set of empirical formulae for estimating the fraction of the protein in different structural motifs based on peak heights at certain wavenumbers, without the need for deconvolution.[174,175] Different formulae apply for ATR-IR and transmission IR.

ATR-IR offers the possibility to study a thin layer of protein deposited on an ATR element, which is appealing since the analysis uses only a tiny amount of protein[175] – $\sim$10 ng compared to 10–100 μg in a 5 μm cell.[173] A further appealing property of ATR-IR is the reduction in path length of the water recorded. However, there are two important differences between transmission IR and ATR-IR spectra.[172,175] First, proteins in adsorbed films may be partially dehydrated which can affect the protein structure. Second, the peaks may shift and change in intensity for purely optical reasons as explained in section 2.3. Goormaghtigh and coworkers dismiss the latter effect as insignificant for thin films,[175] but it still presents a potential complication for thicker films that could lead to the mis-assignment of secondary structures. The possibility of a protein denaturing on the ATR element is a more serious problem; however, if multilayers of protein are used the first layer—directly adsorbed to the surface—either contributes little to the overall spectrum or can be removed by spectral subtraction.[13] Owing to the differences between the spectra of adsorbed layers and proteins in solution, some groups have discouraged the use of ATR-IR for determining protein structure when other methods are possible.[172]

ATR-IR spectroscopy has been used to follow the process of protein adsorption to solid surfaces. At high concentrations some proteins adsorb in multiple layers. Wei *et al.*. studied the adsorption of four such proteins. Initially adsorption is governed by the interaction between the protein and the surface, but once a few layers have been deposited the rate of adsorption tends to a constant value governed by the protein–protein interactions.[176] This change in the chemical environment of adsorption can be followed both by the rate of change of the amount adsorbed, and by the change in secondary structure with time. Figure 20 shows this effect for two different proteins. For simply calculating the amount of protein adsorbed, the protein amide II band (1480–1590) cm^{-1} is most reliable since it is least sensitive to structural rearrangement.[176]

A useful method to make TIR spectroscopy more selective is to functionalise the surface with specific receptors. For TIRF the use of selective surface
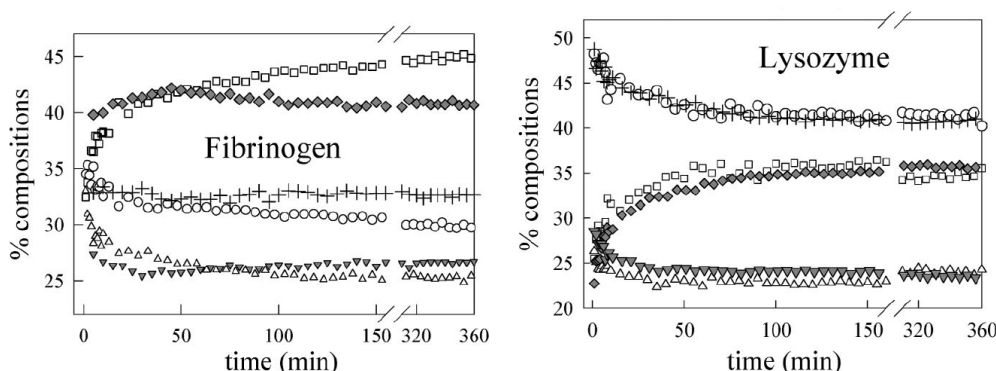
Figure 20: Change of protein secondary structure with time for two proteins adsorbed on a Ge surface, followed with ATR-IR spectroscopy. During this time the protein adsorption is increasing, and the change in structure arises from the contribution of the layers further from the surface. α-helix/random-coil: crosses for Tris-HCl buffer, and open circles for phosphate buffered saline; β-sheets: filled diamonds for Tris-HCl and open squares for phosphate buffered saline; Turns are filled triangles for Tris-HCl and open triangles for phosphate buffered saline. Reprinted with permission from ref. 176. Copyright 2009 American Chemical Society.

was an early development with free antibody concentrations monitored by their ability to bind to surface immobilised proteins.[177] Taitt *et al.* reviewed the rather extensive field.[178] The use of ATR-IR with functionalised surfaces is also reasonably well-developed: ref. 92 provides an overview of the different approaches that can be used, including direct chemical modification of silicon surfaces, gold coating followed by thiol coupling on germanium surfaces, and direct chemical bonding to germanium.

4.3.3 Protein–lipid mixtures

Both ATR-IR and TIRF spectroscopy have been used extensively to study protein–lipid interactions. A common theme of interest is the orientation of the protein inside a membrane. There are a variety of good (though dated) reviews on this subject.[13,179,180] Early work used oriented multilayers, which can be prepared simply by casting lipid dissolved in an organic solvent. These thick films are ideal for studying lipids by themselves, but may not be a good model for membrane proteins, which often have hydrophilic regions that sit outside the bilayer. Lipid bilayers supported on a planar substrate provide a more realistic model of a biological membrane; they are separated from the substrate by a thin film of water (10–20 Å) which prevents too much
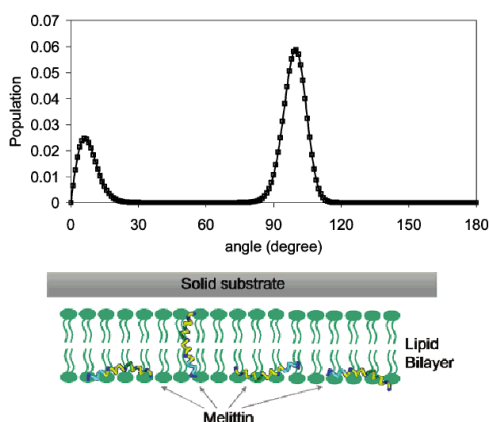
45

Figure 21: Orientation distribution (top) and schematic diagram (bottom) of melittin interacting with a lipid bilayer, deduced using a combination of the order parameters from ATR-IR and sum-frequency generation. Reprinted with permission from ref. 108. Copyright 2007 American Chemical Society.

interaction between a membrane protein and the solid substrate.[179] There are a number of means to prepare supported bilayers. One common method is to deposit a lipid monolayer by Langmuir-Blodgett deposition followed by the adsorption of the second leaflet of the bilayer (of the same or different lipid) from a vesicle solution.[136] If the interaction of the bilayer with the substrate is still perceived to be a problem, the bilayer can be separated from the surface either by tethering it to a self-assembled monolayer or by adsorbing it on a hydrated polymer cushion, allowing membrane proteins to interact with the membrane without interacting with the inorganic substrate.[181,182]

A classic example of an oriented protein within lipid membranes is melittin (a constituent of bee venom). It is known to form a bimodal distribution, with some protein lying parallel to the surface of the bilayer and some spanning the bilayer (see figure 21). An early ATR-IR study of the protein by Frey and Tamm illustrated how modelling a cell membrane with a multilayer stack of bilayers can give misleading results: they found that melittin was preferentially oriented parallel to the plane of a lipid bilayer in D_2O, but parallel to the lipid chains when incorporated in a dry multilayer stack.[103] More recently, Chen and coworkers obtained a more detailed angular distribution using both ATR-IR and sum-frequency spectroscopy.[108] By combining the orientational information obtained with sum-frequency (which probes $\langle \cos\theta \rangle$ and $\langle \cos^3\theta \rangle$) with the $\langle \cos^2\theta \rangle$ distribution obtained with ATR-IR, they were able to confirm the expected bimodal distribution (fig. 21).
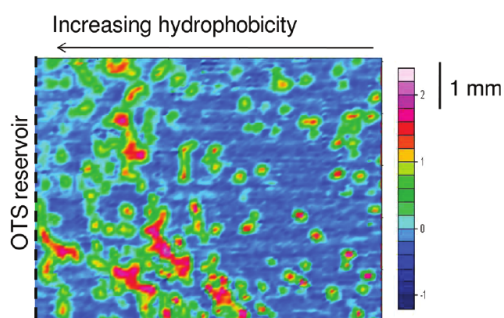
Figure 22: ATR-IR image showing lysozyme crystals formed on a Si ATR element functionalised to give a hydrophobicity gradient. The image is based on the intensity of the protein amide II band. Reprinted with permission from ref. 185. Copyright 2012 American Chemical Society.

4.4 Imaging

TIRF is almost invariably conducted in imaging mode, since a two-dimensional map can be generated by relaying the light from the sample through a filter onto a CCD or CMOS detector. For TIR-Raman and ATR-IR spectroscopies one needs to record spatial information concurrently with spectral information. In ATR-IR, a focal plane array detector is used to acquire an image at each interferometer delay. An interferogram is then reconstructed for each pixel and a Fourier transform employed to generate the IR spectrum.

Kazarian and Chan have recently reviewed biomedical applications of imaging[183,184] and technical aspects.[53] A single-reflection geometry must be used for ATR-IR imaging, limiting the sensitivity. Applications include imaging protein crystallisation (see figure 22),[185] polymer chemistry,[186,187] the distribution of active ingredients within commercial ointments,[188] protein distribution in cartilage,[189,190] the structure and composition of paints used in artworks,[191] and mixing in microfluidic devices.[192] In many of these cases, the short penetration depth simply serves as a convenient two-dimensional slice. Although the whole sample can be imaged simultaneously with the spectra extracted through Fourier transform IR, this process is still slow (∼mins per image) and so where higher time resolution is needed fluorescent labelling might be a better alternative.

Raman imaging could in principle yield higher spatial resolution than ATR-IR due to the shorter wavelengths and the ready availability of high resolution detectors. While Fourier transform Raman imaging is well-established with 1064 nm laser sources, it lacks the sensitivity to map thin films on surfaces. To our knowledge, there has only been one example of imaging by

TIR-Raman,[38] using annular illumination. The image was obtained by moving the position of the sample (a patterned polymer film) under the collection microscope, and hence a different spectrum had to be taken at every point.

4.5   Depth profiling

The idea of using internal reflection spectroscopy for depth profiling is appealing. The penetration depth of the evanescent wave varies with the angle of incidence. For a specific spectral wavelength, ν, the measured signal, $I(\nu, \theta_i)$ depends on a Laplace transform of the sample response with respect to depth, $f(z, \nu)$:

$$I(\nu, \theta_i) \propto E_0(\theta_i) \int_0^\infty f(z, \nu) e^{-2z/d_p(\theta_i)} \, \mathrm{d}z \,, \qquad (28)$$

assuming that the refractive index is constant with depth. (Eq. 28 above applies to Raman scattering and fluorescence and is a reasonable approximation for weakly absorbing samples in ATR spectroscopies; for strongly absorbing samples the relationship is more complex, see for example ref. 193.) In principle, $f(z, \nu)$, can be recovered uniquely through an inverse Laplace transform of the $I(\nu, \theta_i)$ with respect to the inverse penetration depth. In reality, however, it is only possible to fit the concentration profile to simple models—for example a layered system with well-defined layers or an exponential decay in concentration—and it is almost impossible to distinguish definitively between different models. We discussed this issue in more detail in our recent review of TIR Raman scattering,[3] and Power has written an extensive review of the problem of recovering depth profiles from spectroscopic techniques.[194] The principal difficulty is that the form of the evanescent field does not vary strongly with angle of incidence, except very close to the critical angle so each different angle of incidence imparts very little new information. Near θ_c, the finite numerical aperture of the excitation beam averages over a wide range of different penetration depths, further degrading the quality of the depth information (see figure 3 earlier for an illustration of the spread of incident angles from various numerical apertures).

In the 1980s and 1990s, considerable effort was invested in the problems of highly absorbing materials and variable refractive indices in ATR-IR depth profiling.[193,196] This work did not usually try to perform the inverse Laplace transform directly, but instead fitted the intensity data to a model concentration profile.[196,197] Recently Kazarian and coworkers have combined depth profiling with imaging,[195,198] in order to extract qualitative information about the thickness of layers and the order in which they occur; figure 23 shows an example of the imaging of multiple polymer layers. This qualitative
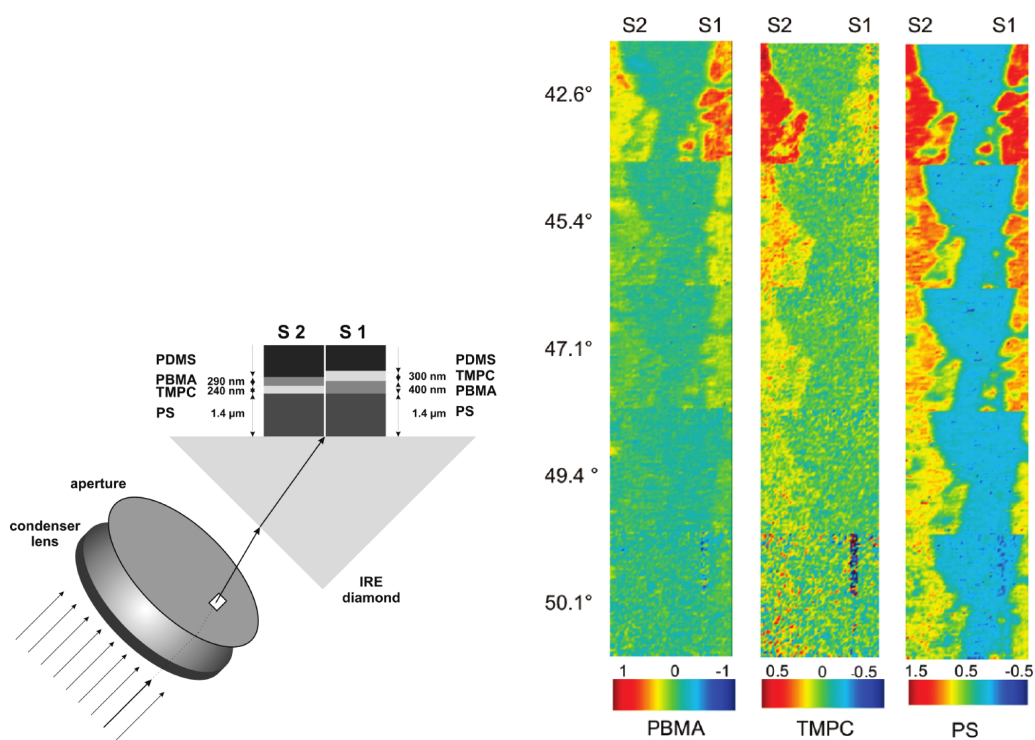
Figure 23: Schematic of a variable angle ATR-IR imaging experiment, showing two different polymer stacks, and images taken with different angles of incidence. Higher angles of incidence probe a thinner cross-section of sample. Reprinted with permission from ref. 195. Copyright 2010 American Chemical Society.

approach probably represents the sensible limitation of depth profiling by internal reflection spectroscopy. TIRF depth profiling has followed a similar pattern to ATR-IR: either data are fitted to simple models[199–202] (with no real way of verifying the accuracy of the model) or only qualitative conclusions are drawn.[203] There has only been very limited work on depth profiling by TIR-Raman: Fontaine and Furtak published a pair of papers on experimental considerations,[204] and on measurements from a simple two-layer polymer film,[205] while Smith and coworkers investigated the precision with which TIR Raman can measure the thickness of a single polymer film.[206]

Total reflection X-ray fluorescence has also been used for depth profiling,[207] for example, the counterion distribution in Langmuir-Blodgett films.[208] XRF suffers from the same limitations as other total internal reflection techniques.

4.6 Other applications

In this final section, we highlight a few interesting applications relating to topical problems in soft matter.

A pair of studies used evanescent-wave Raman spectroscopy to look at orientation near the surface of liquid crystals[86,209] (ref. 209 used waveguide rather than TIR illumination). These studies are notable for two reasons: first, the use of a transparent electrode as the optical interface allowed the application of an electric field to the sample (although some of the early TIR Raman studies also used transparent electrode interfaces for cyclic voltammetry measurements[29]). Second, the studies demonstrate fine (μs) time resolution by using a short laser pulse—slightly offset from the application of the electric field—and integrating over many such pulses. Obviously this approach requires an experiment that is reproducible over multiple perturbations. Similarly, Noda and coworkers averaged over multiple ATR-IR spectra while applying a sinusoidally varying pressure at 2500 Hz to a PET polymer film.[210] An example is shown in figure 24, in which the variation of the IR signal with time does not directly follow the form of the applied pressure.

TIR Raman spectroscopy has been used to study the properties of lubricants under pressure, both for boundary lubricants[4] and fluid liquid films.[212] In both cases the lubricating film is placed between the internal reflection element and another substrate (see figure 25) and the pressure between the two solids increased. Related experiments have been conducted using ATR-IR,[213] IR reflection-absorption[214] and confocal Raman spectroscopies.[215] There are a number of specific advantages to TIR Raman spectroscopy for this experiment. First, the small sample area of TIR-Raman is beneficial, since a small area makes it easier to reach high pressures; ATR-IR does not cur-
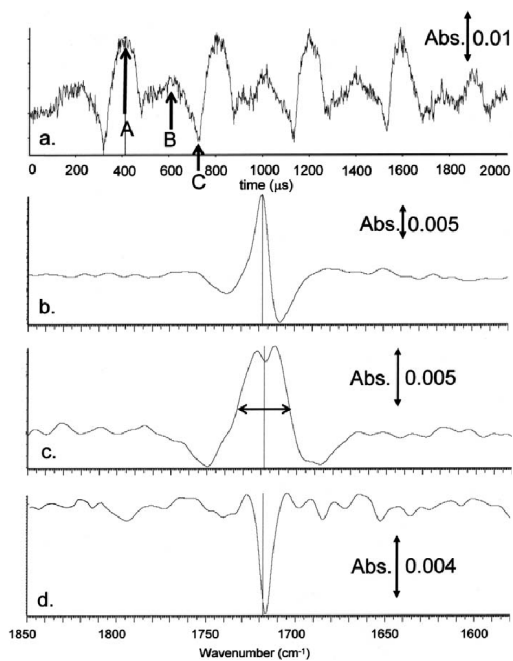
Figure 24: (a) Intensity of the $1719\,\mathrm{cm}^{-1}$ C=O stretching band of PET, with respect to time for $2500\,\mathrm{Hz}$ sinusoidal compressions (the equivalent plot for the C-O stretching band at $1255\,\mathrm{cm}^{-1}$, not shown here, showed a sinusoidal response). (b-d), difference spectra from the mean spectrum taken at the times indicated as A, B and C respectively. Reprinted with permission from ref. 210. Copyright 2012 the Society for Applied Spectroscopy.
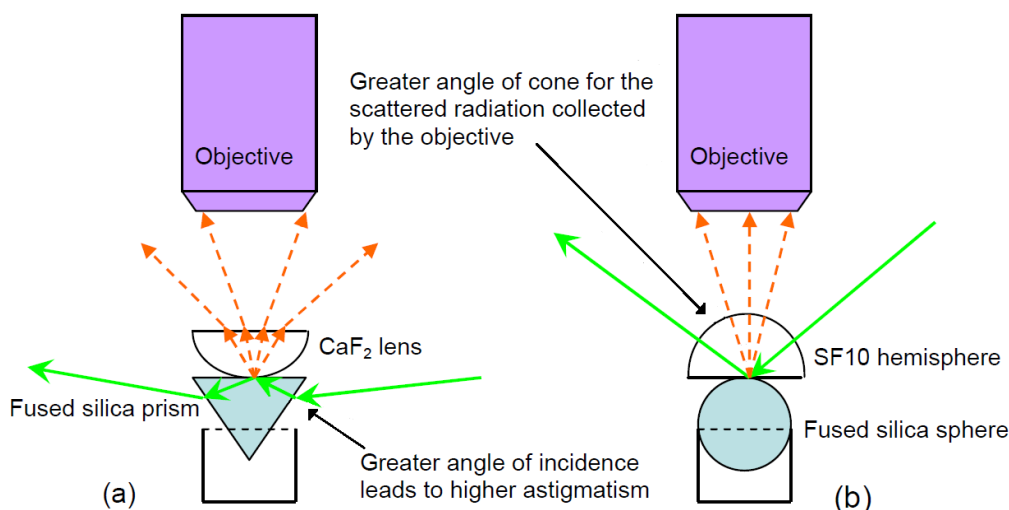
Figure 25: Schematic diagram of two different experimental set-ups used for TIR-Raman tribology studies. Adapted from ref. 211 with kind permission.

rently have the necessary sensitivity in a single-reflection geometry. Second, the enhancement from the evanescent wave increases the signal (compared to confocal Raman); and third, the controlled polarisation of TIR-Raman provides more information on the tilt of the lubricating molecules than is available in confocal Raman. ATR-IR spectroscopy is viable for studying thicker films under less confined conditions:[213] figure 26 illustrates a cylinder sliding along a multiple reflection ATR crystal. Chemical reactions in the oil following hours of wear could be detected through the changes in the ATR-IR spectrum. Cann has recently reviewed the (linear) spectroscopic techniques available for studying tribological films.[216]

Zhang and coworkers recently used ATR-IR to investigate the presence of the gaseous nanobubbles at the hydrophobic solid–water interface.[217] Structures interpreted as nanobubbles had previously been observed by AFM imaging, however the identification was based on shape since AFM provides no information on the composition or state of the features observed. The possibility also existed that the AFM tip was inducing the formation of bubbles. Bubbles of CO_2 gas at the interface could be identified definitively by ATR-IR, since CO_2 has a dramatically different spectrum in the gas state and in an aqueous solution. The volume of the bubble was calculated from the loss of D_2O compared to a bubble-free surface. The pressure inside the bubbles was calculated either from the CO_2 peak intensity and the volume or from the line width of the gaseous CO_2 (although the accuracy of the latter
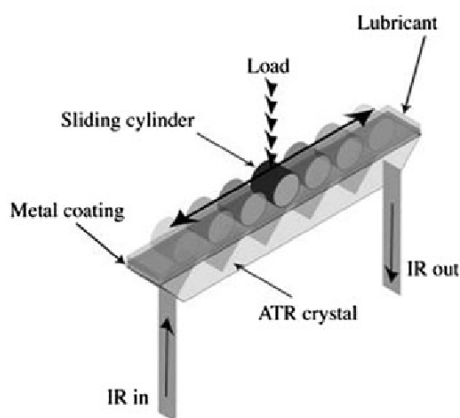
Figure 26: ATR-IR tribological apparatus: a cylinder is slid along an ATR element coated with metal and a lubricant. Reprinted from ref 213, with kind permission from Springer Science and Business Media.

method was limited by the resolution of the instrument).

5 Conclusions

The use of evanescent waves to make bulk spectroscopic techniques surface-sensitive dates back more than half a century. Many different forms of spectroscopy, including IR and UV/vis absorption, Raman scattering and fluorescence, have exploited the benefits offered by total internal reflection. This review has been aimed at soft matter researchers who may have a familiarity with bulk spectroscopy but who are not experts in TIR techniques. We have set out the principles, instrumentation and applications of TIR spectroscopy at a depth that will enable readers to read the soft matter literature critically and to assess the usefulness of TIR spectroscopy for applications of interest to them. We have tried to highlight limitations and pitfalls in a disinterested way. The level of detail is not sufficient for researchers to embark on TIR spectroscopy on the basis of this review alone, but pointers to the detailed literature are provided. The examples provided are chosen to be illustrative and this review does not purport to provide comprehensive coverage of the literature: references to more extensive and specialised review articles have been provided. TIR spectroscopies are a powerful set of techniques; we hope this review will lead to them being adopted ever more widely to study soft matter at interfaces.

References

[1] P. L. Stiles, J. A. Dieringer, N. C. Shah and R. P. Van Duyne, *Annual Review of Analytical Chemistry*, 2008, **1**, 601–626.

[2] A. Kudelski, *Surface Science*, 2009, **603**, 1328–1334.

[3] D. A. Woods and C. D. Bain, *Analyst*, 2012, **137**, 35–48.

[4] D. A. Beattie, S. Haydock and C. D. Bain, *Vibrational Spectroscopy*, 2000, **24**, 109–123.

[5] W. N. Hansen, *J. Opt. Soc. Am.*, 1968, **58**, 380–388.

[6] T. Burghardt and D. Axelrod, *Biophysical Journal*, 1981, **33**, 455–467.

[7] G. Müller, K. Abraham and M. Schaldach, *Appl. Opt.*, 1981, **20**, 1182–1190.

[8] W. N. Hansen, *Spectrochimica Acta*, 1965, **21**, 815–833.

[9] J. E. Bertie, M. K. Ahmed and H. H. Eysel, *The Journal of Physical Chemistry*, 1989, **93**, 2210–2218.

[10] M. D. Porter, T. B. Bright, D. L. Allara and T. Kuwana, *Analytical Chemistry*, 1986, **58**, 2461–2465.

[11] L. W. Pinkley, P. P. Sethna and D. Williams, *The Journal of Physical Chemistry*, 1978, **82**, 1532–1537.

[12] N. J. Harrick, *Internal Reflection Spectroscopy*, John Wiley & Sons, Inc., 1967.

[13] E. Goormaghtigh, V. Raussens and J.-M. Ruysschaert, *Biochimica et Biophysica Acta (BBA) - Reviews on Biomembranes*, 1999, **1422**, 105–185.

[14] N. J. Harrick, *J. Opt. Soc. Am.*, 1965, **55**, 851–856.

[15] K. Yamamoto and H. Ishida, *Vibrational Spectroscopy*, 1994, **8**, 1–36.

[16] J. E. Bertie, in *Handbook of Vibrational Spectroscopy*, John Wiley & Sons, Ltd, 2006, ch. Optical Constants.

[17] J. Huang and M. Urban, *Applied Spectroscopy*, 1992, **46**, 1666–1672.

[18] K. Ohta and H. Ishida, *Applied Spectroscopy*, 1988, **42**, 952–957.

[19] M. J. Dignam and S. Mamiche-Afara, *Spectrochimica Acta Part A: Molecular Spectroscopy*, 1988, **44**, 1435–1442.

[20] F. Picard, T. Buffeteau, B. Desbat, M. Auger and M. Pézolet, *Biophysical Journal*, 1999, **76**, 539–551.

[21] D. Axelrod, *Journal of Biomedical Optics*, 2001, **6**, 6–13.

[22] W. P. Ambrose, P. M. Goodwin and J. P. Nolan, *Cytometry*, 1999, **36**, 224–231.

[23] J. W. M. Chon and M. Gu, *Appl. Opt.*, 2004, **43**, 1063–1071.

[24] G. Terakado, K. Watanabe and H. Kano, *Appl. Opt.*, 2009, **48**, 1114–1118.

[25] M. Oheim and F. Schapper, *Journal of Physics D: Applied Physics*, 2005, **38**, R185.

[26] M. Leutenegger, C. Ringemann, T. Lasser, S. W. Hell and C. Eggeling, *Opt. Express*, 2012, **20**, 5243–5263.

[27] E. Tyrode, M. W. Rutland and C. D. Bain, *Journal of the American Chemical Society*, 2008, **130**, 17434–17445.

[28] T. Ikeshoji, Y. Ono and T. Mizuno, *Appl. Opt.*, 1973, **12**, 2236–2237.

[29] M. Fujihira and T. Osa, *Journal of the American Chemical Society*, 1976, **98**, 7850–7851.

[30] T. Takenaka and K. Yamasaki, *Journal of Colloid and Interface Science*, 1980, **78**, 37–43.

[31] T. Takenaka and H. Fukuzaki, *Journal of Raman Spectroscopy*, 1979, **8**, 151–154.

[32] T. Takenaka and T. Nakanaga, *The Journal of Physical Chemistry*, 1976, **80**, 475–480.

[33] T. Nakanaga and T. Takenaka, *The Journal of Physical Chemistry*, 1977, **81**, 645–649.

[34] R. Iwamoto, M. Miya, K. Ohta and S. Mima, *Journal of the American Chemical Society*, 1980, **102**, 1212–1213.

[35] R. Iwamoto, M. Miya, K. Ohta and S. Mima, *Journal of Chemical Physics*, 1981, **74**, 4780–4790.

[36] D. A. Woods, J. Petkov and C. D. Bain, *The Journal of Physical Chemistry B*, 2011, **115**, 7341–7352.

[37] L. G. Tisinger and A. J. Sommer, *Microscopy and Microanalysis*, 2004, **10**, 1318–1319.

[38] C. A. Michaels, *Journal of Raman Spectroscopy*, 2010, **41**, 1670–1677.

[39] A. G. Tweet, J. G. L. Gaines and W. D. Bellamy, *The Journal of Chemical Physics*, 1964, **40**, 2596–2600.

[40] T. Hirschfeld, *Canadian Spectroscopy*, 1965, **10**, 128.

[41] A. L. Stout and D. Axelrod, *Appl. Opt.*, 1989, **28**, 5237–5242.

[42] E. H. Hellen and D. Axelrod, *Journal of Fluorescence*, 1991, **1**, 113–128.

[43] N. Thompson, T. Burghardt and D. Axelrod, *Biophysical Journal*, 1981, **33**, 435–454.

[44] D. Toomre and D. J. Manstein, *Trends in Cell Biology*, 2001, **11**, 298–303.

[45] D. Axelrod, *Traffic*, 2001, **2**, 764–774.

[46] A. L. Mattheyses, S. M. Simon and J. Z. Rappoport, *Journal of Cell Science*, 2010, **123**, 3621–3628.

[47] M. Toriumi, S. Saito, K. Kawaguchi and K. Aiki, *Review of Scientific Instruments*, 1995, **66**, 3520–3526.

[48] J. Koo and C. Czeslik, *Review of Scientific Instruments*, 2012, **83**, 085109.

[49] I. Gryczynski, Z. Gryczynski and J. R. Lakowicz, *Analytical Biochemistry*, 1997, **247**, 69–76.

[50] G. Mashanov, D. Tacon, A. Knight, M. Peckham and J. E. Molloy, *Methods*, 2003, **29**, 142–152.

[51] M. J. Rust, M. Bates and X. Zhuang, *Nature methods*, 2006, **3**, 793–795.

[52] A. R. Hind, S. K. Bhargava and A. McKinnon, *Advances in Colloid and Interface Science*, 2001, **93**, 91–114.

[53] S. G. Kazarian and K. L. A. Chan, *Applied Spectroscopy*, 2010, **64**, 135A–151A.

[54] M. Milosevic, N. J. Harrick and S. L. Berets, *Applied Spectroscopy*, 1991, **45**, 126–131.

[55] J. Fahrenfort, *Spectrochimica Acta*, 1961, **17**, 698–709.

[56] N. J. Harrick, *Phys. Rev. Lett.*, 1960, **4**, 224–226.

[57] N. J. Harrick, *The Journal of Physical Chemistry*, 1960, **64**, 1110–1114.

[58] H. Danigel, *Optical Engineering*, 1995, **34**, 2665–2669.

[59] N. Higashi, A. Ikehata and Y. Ozaki, *Review of Scientific Instruments*, 2007, **78**, 103107.

[60] K. A. Lee and D. C. Rich, *Applied Spectroscopy*, 2011, **65**, 326–333.

[61] L. van der Sneppen, G. Hancock, C. Kaminski, T. Laurila, S. R. Mackenzie, S. R. T. Neil, R. Peverall, G. A. D. Ritchie, M. Schnippering and P. R. Unwin, *Analyst*, 2010, **135**, 133–139.

[62] L. van der Sneppen, F. Ariese, C. Gooijer and W. Ubachs, *Annual Review of Analytical Chemistry*, 2009, **2**, 13–35.

[63] M. Schnippering, S. R. T. Neil, S. R. Mackenzie and P. R. Unwin, *Chem. Soc. Rev.*, 2011, **40**, 207–220.

[64] A. M. Shaw, T. E. Hannon, F. Li and R. N. Zare, *The Journal of Physical Chemistry B*, 2003, **107**, 7070–7075.

[65] I. M. P. Aarts, A. C. R. Pipino, J. P. M. Hoefnagels, W. M. M. Kessels and M. C. M. van de Sanden, *Phys. Rev. Lett.*, 2005, **95**, 166104.

[66] J. Scherer, D. Voelkel, D. Rakestraw, J. Paul, C. Collier, R. Saykally and A. O'Keefe, *Chemical Physics Letters*, 1995, **245**, 273–280.

[67] W. B. Yun and J. M. Bloch, *Journal of Applied Physics*, 1990, **68**, 1421–1428.

[68] R. Klockenkämper, *Spectrochimica Acta Part B: Atomic Spectroscopy*, 2006, **61**, 1082–1090.

[69] H. Tanida, *Spectrochimica Acta Part B: Atomic Spectroscopy*, 2004, **59**, 1071–1076.

[70] P. Wobrauschek, *X-Ray Spectrometry*, 2007, **36**, 289–300.

[71] V. L. Shapovalov, M. E. Ryskin, O. V. Konovalov, A. Hermelink and G. Brezesinski, *The Journal of Physical Chemistry B*, 2007, **111**, 3927–3934.

[72] M. Newville, *Fundamentals of XAFS*, University of Chicago, `http://www.xafs.org/Tutorials?action=AttachFile&do=get&target=Newvillexasfundamentals.pdf`, 2004.

[73] H. Tanida, H. Nagatani and M. Harada, *Journal of Physics: Conference Series*, 2009, **190**, 012061.

[74] H. Tanida, H. Nagatani and M. Harada, *Journal of Physics: Conference Series*, 2007, **83**, 012019.

[75] Y. R. Shen, *Nature*, 1989, **337**, 519–525.

[76] F. M. Geiger, *Annual Review of Physical Chemistry*, 2009, **60**, 61–83.

[77] C. T. Williams, Y. Yang and C. D. Bain, *Langmuir*, 2000, **16**, 2343–2350.

[78] G. I. Stegeman, R. Fortenberry, C. Karaguleff, R. Moshrefzadeh, W. M. Hetherington, III, N. E. Van Wyck and J. E. Sipe, *Opt. Lett.*, 1983, **8**, 295–297.

[79] W. M. K. P. Wijekoon, Z. Z. Ho and W. M. Hetherington, *J. Chem. Soc., Faraday Trans.*, 1993, **89**, 1067–1069.

[80] H. Yui, H. Fujiwara and T. Sawada, *Chemical Physics Letters*, 2002, **360**, 53–58.

[81] C. L. Evans and X. S. Xie, *Annual Review of Analytical Chemistry*, 2008, **1**, 883–909.

[82] R. Sjöback, J. Nygren and M. Kubista, *Spectrochimica Acta Part A: Molecular and Biomolecular Spectroscopy*, 1995, **51**, L7–L21.

[83] C.-G. Gölander, V. Hlady, K. Caldwell and J. Andrade, *Colloids and*

Surfaces, 1990, **50**, 113–130.

[84] J. Oreopoulos and C. M. Yip, *Biophysical Journal*, 2009, **96**, 1970–1984.

[85] D. A. Woods, J. Petkov and C. D. Bain, *Colloids and Surfaces A: Physicochemical and Engineering Aspects*, 2011, **391**, 10–18.

[86] T. Morikawa, E. Shirai, J. Tanno, H. Takanashi, A. Yasuda and K. Itoh, *Molecular Crystals and Liquid Crystals Science and Technology. Section A. Molecular Crystals and Liquid Crystals*, 1998, **312**, 69–94.

[87] R. P. Sperline, J. S. Jeon and S. Raghavan, *Applied Spectroscopy*, 1995, **49**, 1178–1182.

[88] R. Maoz and J. Sagiv, *Journal of Colloid and Interface Science*, 1984, **100**, 465–496.

[89] R. Banga, J. Yarwood, A. M. Morgan, B. Evans and J. Kells, *Langmuir*, 1995, **11**, 4393–4399.

[90] M. Bieri and T. Bürgi, *The Journal of Physical Chemistry B*, 2005, **109**, 10243–10250.

[91] M. Voue, E. Goormaghtigh, F. Homble, J. Marchand-Brynaert, J. Conti, S. Devouge and J. De Coninck, *Langmuir*, 2007, **23**, 949–955.

[92] C. Vigano, J.-M. Ruysschaert and E. Goormaghtigh, *Talanta*, 2005, **65**, 1132–1142.

[93] A. J. McQuillan, *Advanced Materials*, 2001, **13**, 1034–1038.

[94] D. Beattie, M. Lidström Larsson and A. R. Holmgren, *Vibrational Spectroscopy*, 2006, **41**, 198–204.

[95] G. W. Faris and R. A. Copeland, *Appl. Opt.*, 1997, **36**, 2686–2688.

[96] M. O. Trulson and R. A. Mathies, *The Journal of Chemical Physics*, 1986, **84**, 2068–2074.

[97] W. K. Thompson, *Trans. Faraday Soc.*, 1965, **61**, 2635–2640.

[98] A. E. Klingbeil, J. B. Jeffries and R. K. Hanson, *Journal of Quantitative Spectroscopy and Radiative Transfer*, 2007, **107**, 407–420.

[99] V. A. Rebar and M. M. Santore, *Macromolecules*, 1996, **29**, 6262–6272.

[100] N. L. Thomson, K. H. Pearce and H. V. Hsieh, *European Biophysics Journal*, 1993, **22**, 367–378.

[101] R. P. Sperline, S. Muralidharan and H. Freiser, *Langmuir*, 1987, **3**, 198–202.

[102] P. K. Singh, J. J. Adler, Y. I. Rabinovich and B. M. Moudgil, *Langmuir*, 2001, **17**, 468–473.

[103] S. Frey and L. Tamm, *Biophysical Journal*, 1991, **60**, 922–930.

[104] K. Rothschild and N. Clark, *Biophysical Journal*, 1979, **25**, 473–487.

[105] R. P. Sperline, Y. Song and H. Freiser, *Langmuir*, 1992, **8**, 2183–2191.

[106] X. Zhai and J. Kleijn, *Biophysical Journal*, 1997, **72**, 2651–2659.

[107] A. F. Runge, S. S. Saavedra and S. B. Mendes, *The Journal of Physical Chemistry B*, 2006, **110**, 6721–6731.

[108] X. Chen, J. Wang, A. P. Boughton, C. B. Kristalyn and Z. Chen, *Journal of the American Chemical Society*, 2007, **129**, 1420–1427.

[109] H. Li and C. P. Tripp, *Langmuir*, 2002, **18**, 9441–9446.

[110] R. F. Tabor, J. Eastoe and P. Dowding, *Langmuir*, 2009, **25**, 9785–9791.

[111] W. J. Lokar and W. A. Ducker, *Langmuir*, 2004, **20**, 4553–4558.

[112] H. Li and C. P. Tripp, *The Journal of Physical Chemistry B*, 2004, **108**, 18318–18326.

[113] D. J. Neivandt, M. L. Gee, C. P. Tripp and M. L. Hair, *Langmuir*, 1997, **13**, 2519–2526.

[114] D. A. Woods, J. Petkov and C. D. Bain, *The Journal of Physical Chemistry B*, 2011, **115**, 7353–7363.

[115] R. P. Sperline, Y. Song and H. Freiser, *Langmuir*, 1997, **13**, 3727–3732.

[116] R. Wirz, T. Bürgi and A. Baiker, *Langmuir*, 2003, **19**, 785–792.

[117] D. Baurecht and U. P. Fringeli, *Review of Scientific Instruments*, 2001, **72**, 3782–3792.

[118] D. J. Neivandt, M. L. Gee, M. L. Hair and C. P. Tripp, *The Journal of Physical Chemistry B*, 1998, **102**, 5107–5114.

[119] R. F. Tabor, J. Eastoe and P. Dowding, *Langmuir*, 2010, **26**, 671–677.

[120] P. A. Connor and A. J. McQuillan, *Langmuir*, 1999, **15**, 2916–2921.

[121] A. Couzis and E. Gulari, *Langmuir*, 1993, **9**, 3414–3421.

[122] C. F. Wertz and M. M. Santore, *Langmuir*, 1999, **15**, 8884–8894.

[123] A. Toscano and M. M. Santore, *Langmuir*, 2006, **22**, 2588–2597.

[124] K. E. Sapsford and F. S. Ligler, *Biosensors and Bioelectronics*, 2004, **19**, 1045–1055.

[125] S. M. Daly, T. M. Przybycien and R. D. Tilton, *Langmuir*, 2005, **21**, 1328–1337.

[126] D. Parsons, R. Harrop and E. Mahers, *Colloids and Surfaces*, 1992, **64**, 151–160.

[127] Z. Fu and M. M. Santore, *Macromolecules*, 1998, **31**, 7014–7022.

[128] S. C. Clark and W. A. Ducker, *The Journal of Physical Chemistry B*, 2003, **107**, 9011–9021.

[129] A. Khan, W. A. Ducker and M. Mao, *The Journal of Physical Chemistry B*, 2006, **110**, 23365–23372.

[130] E. R. Malinowski, *Factor Analysis in Chemistry*, John Wiley & Sons, 2nd edn., 1991.

[131] N. L. Thompson, X. Wang and P. Navaratnarajah, *Journal of Structural Biology*, 2009, **168**, 95–106.

[132] R. L. Hansen and J. M. Harris, *Analytical Chemistry*, 1998, **70**, 4247–4256.

[133] A. M. Lieto, R. C. Cush and N. L. Thompson, *Biophysical Journal*, 2003, **85**, 3294–3302.

[134] K. S. McCain, P. Schluesche and J. M. Harris, *Analytical Chemistry*, 2004, **76**, 930–938.

[135] A. W. Sonesson, H. Blom, K. Hassler, U. M. Elofsson, T. H. Callisen, J. Widengren and H. Brismar, *Journal of Colloid and Interface Science*, 2008, **317**, 449–457.

[136] E. Kalb, S. Frey and L. K. Tamm, *Biochimica et Biophysica Acta (BBA) - Biomembranes*, 1992, **1103**, 307–316.

[137] V. Chan, D. J. Graves, P. Fortina and S. E. McKenzie, *Langmuir*, 1997, **13**, 320–329.

[138] B. Kannan, L. Guo, T. Sudhaharan, S. Ahmed, I. Maruyama and T. Wohland, *Analytical Chemistry*, 2007, **79**, 4463–4470.

[139] L. Guo, J. Y. Har, J. Sankaran, Y. Hong, B. Kannan and T. Wohland, *ChemPhysChem*, 2008, **9**, 721–728.

[140] W. B. Martin, S. Mirov, D. Martyshkin, R. Venugopalan and A. M. Shaw, *Journal of Biomedical Optics*, 2005, **10**, 024025.

[141] M. A. Everest, V. M. Black, A. S. Haehlen, G. A. Haveman, C. J. Kliewer and H. A. Neill, *The Journal of Physical Chemistry B*, 2006, **110**, 19461–19468.

[142] M.-S. Chen, H.-F. Fan and K.-C. Lin, *Analytical Chemistry*, 2010, **82**, 868–877.

[143] H. V. Powell, M. Schnippering, M. Mazurenka, J. V. Macpherson, S. R. Mackenzie and P. R. Unwin, *Langmuir*, 2009, **25**, 248–255.

[144] R. Haselberg, L. van der Sneppen, F. Ariese, W. Ubachs, C. Gooijer, G. J. de Jong and G. W. Somsen, *Analytical Chemistry*, 2009, **81**, 10172–10178.

[145] K. Fujiwara and H. Watarai, *Langmuir*, 2003, **19**, 2658–2664.

[146] S. Yamamoto and H. Watarai, *The Journal of Physical Chemistry C*, 2008, **112**, 12417–12424.

[147] R. P. Sperline and H. Freiser, *Langmuir*, 1990, **6**, 344–347.

[148] S. Ishizaka, H.-B. Kim and N. Kitamura, *Analytical Chemistry*, 2001, **73**, 2421–2428.

[149] R. Walder and D. K. Schwartz, *Soft Matter*, 2011, **7**, 7616–7622.

[150] J. Perera and G. Stevens, *Analytical and Bioanalytical Chemistry*, 2009, **395**, 1019–1032.

[151] T. Satoshi, *Analytica Chimica Acta*, 2006, **556**, 16–25.

[152] Y. Katsumoto, T. Tanaka, H. Sato and Y. Ozaki, *The Journal of Physical Chemistry A*, 2002, **106**, 3429–3435.

[153] D. J. Walls and J. C. Coburn, *Journal of Polymer Science Part B: Polymer Physics*, 1992, **30**, 887–897.

[154] K. R. Kirov and H. E. Assender, *Macromolecules*, 2005, **38**, 9258–9265.

[155] H. H. Chuah, *Macromolecules*, 2001, **34**, 6985–6993.

[156] M. Ide, T. Mori, K. Ichikawa, H. Kitano, M. Tanaka, A. Mochizuki, H. Oshiyama and W. Mizuno, *Langmuir*, 2003, **19**, 429–435.

[157] Y. A. Elabd, M. G. Baschetti and T. A. Barbari, *Journal of Polymer Science Part B: Polymer Physics*, 2003, **41**, 2794–2807.

[158] D. T. Hallinan and Y. A. Elabd, *The Journal of Physical Chemistry B*, 2007, **111**, 13221–13230.

[159] M. R. Pereira and J. Yarwood, *J. Chem. Soc., Faraday Trans.*, 1996, **92**, 2731–2735.

[160] M. R. Pereira and J. Yarwood, *J. Chem. Soc., Faraday Trans.*, 1996, **92**, 2737–2743.

[161] C. Sammon, C. Mura, J. Yarwood, N. Everall, R. Swart and D. Hodge, *The Journal of Physical Chemistry B*, 1998, **102**, 3402–3411.

[162] L.-M. Döppers, C. Breen and C. Sammon, *Vibrational Spectroscopy*, 2004, **35**, 27–32.

[163] M. Hartmann, B. D. Hanh, H. Podhaisky, J. Wensch, J. Bodzenta, S. Wartewig and R. H. H. Neubert, *Analyst*, 2004, **129**, 902–905.

[164] C. Lee, H. Wacklin and C. D. Bain, *Soft Matter*, 2009, **5**, 568–575.

[165] M. Käsbauer, M. Junglas and T. Bayerl, *Biophysical Journal*, 1999, **76**, 2600–2605.

[166] H. V. Powell, M. A. O'Connell, M. Zhang, S. R. Mackenzie and P. R.

Unwin, *Analytical Chemistry*, 2012, **84**, 2585–2591.

[167] M. Fix, T. J. Melia, J. K. Jaiswal, J. Z. Rappoport, D. You, T. H. Söllner, J. E. Rothman and S. M. Simon, *Proceedings of the National Academy of Sciences of the United States of America*, 2004, **101**, 7311–7316.

[168] C. Lee and C. D. Bain, *Biochimica et Biophysica Acta (BBA) - Biomembranes*, 2005, **1711**, 59–71.

[169] J. E. Shaw, A. Slade and C. M. Yip, *Journal of the American Chemical Society*, 2003, **125**, 11838–11839.

[170] V. Kiessling, M. K. Domanska, D. Murray, C. Wan and L. K. Tamm, in *Wiley Encyclopedia of Chemical Biology, Volume 4*, John Wiley & Sons, 2008, ch. Supported Lipid Bilayers: Development and Application in Chemical Biology, pp. 411–422.

[171] W. K. Surewicz, H. H. Mantsch and D. Chapman, *Biochemistry*, 1993, **32**, 389–394.

[172] M. Jackson and H. H. Mantsch, *Critical Reviews in Biochemistry and Molecular Biology*, 1995, **30**, 95–120.

[173] A. Barth, *Biochimica et Biophysica Acta (BBA) - Bioenergetics*, 2007, **1767**, 1073–1101.

[174] E. Goormaghtigh, J.-M. Ruysschaert and V. Raussens, *Biophysical Journal*, 2006, **90**, 2946–2957.

[175] E. Goormaghtigh, R. Gasper, A. Bénard, A. Goldsztein and V. Raussens, *Biochimica et Biophysica Acta (BBA) - Proteins & Proteomics*, 2009, **1794**, 1332–1343.

[176] T. Wei, S. Kaewtathip and K. Shing, *The Journal of Physical Chemistry C*, 2009, **113**, 2053–2062.

[177] M. N. Kronick and W. A. Little, *Journal of Immunological Methods*, 1975, **8**, 235–240.

[178] C. R. Taitt, G. P. Anderson and F. S. Ligler, *Biosensors and Bioelectronics*, 2005, **20**, 2470–2487.

[179] L. K. Tamm and S. A. Tatulian, *Quarterly Reviews of Biophysics*, 1997, **30**, 365–429.

[180] S. A. Tatulian, *Biochemistry*, 2003, **42**, 11898–11907.

[181] E. Sackmann and M. Tanaka, *Trends in Biotechnology*, 2000, **18**, 58–64.

[182] M. Tanaka and E. Sackmann, *Nature*, 2005, **437**, 656–663.

[183] S. Kazarian and K. Chan, *Biochimica et Biophysica Acta (BBA) -*

Biomembranes, 2006, **1758**, 858–867.

[184] S. G. Kazarian and K. L. A. Chan, *Analyst*, 2013, **138**, 1940–1951.

[185] S. Glassford, K. L. A. Chan, B. Byrne and S. G. Kazarian, *Langmuir*, 2012, **28**, 3174–3179.

[186] A. Gupper, P. Wilhelm, M. Schmied, S. Kazarian, K. Chan and J. Reußner, *Applied Spectroscopy*, 2002, **56**, 1515–1523.

[187] D. J. Nagle, G. A. George, L. Rintoul and P. M. Fredericks, *Vibrational Spectroscopy*, 2010, **53**, 24–27.

[188] Y. Yamamoto, T. Fukami, T. Koide, T. Suzuki, Y. Hiyama and K. Tomono, *International Journal of Pharmaceutics*, 2012, **426**, 54–60.

[189] J. Yin and Y. Xia, *Applied Spectroscopy*, 2010, **64**, 1199–1208.

[190] J. Yin, Y. Xia and M. Lu, *Spectrochimica Acta Part A: Molecular and Biomolecular Spectroscopy*, 2012, **88**, 90–96.

[191] M. Spring, C. Ricci, D. Peggie and S. Kazarian, *Analytical and Bioanalytical Chemistry*, 2008, **392**, 37–45.

[192] K. L. A. Chan, S. Gulati, J. B. Edel, A. J. de Mello and S. G. Kazarian, *Lab Chip*, 2009, **9**, 2909–2913.

[193] S. Ekgasit and H. Ishida, *Applied Spectroscopy*, 1 September 1996, **50**, 1187–1195.

[194] J. F. Power, *Review of Scientific Instruments*, 2002, **73**, 4057–4141.

[195] T. Frosch, K. L. A. Chan, H. C. Wong, J. T. Cabral and S. G. Kazarian, *Langmuir*, 2010, **26**, 19027–19032.

[196] L. J. Fina and G. Chen, *Vibrational Spectroscopy*, 1991, **1**, 353–361.

[197] R. A. Shick, J. L. Koenig and H. Ishida, *Applied Spectroscopy*, 1 August 1996, **50**, 1082–1088.

[198] K. L. A. Chan and S. G. Kazarian, *Applied Spectroscopy*, January 2007, **61**, 48–54.

[199] W. Reichert, P. Suci, J. Ives and J. Andrade, *Applied Spectroscopy*, 1987, **41**, 503–508.

[200] M. Yanagimachi, M. Toriumi and H. Masuhara, *Appl. Spectrosc.*, 1992, **46**, 832–840.

[201] K. Bessho, T. Uchida, A. Yamauchi, T. Shioya and N. Teramae, *Chemical Physics Letters*, 1997, **264**, 381–386.

[202] B. Olveczky, N. Periasamy and A. Verkman, *Biophysical Journal*, 1997, **73**, 2836–2847.

[203] V. M. Rangnekar and P. B. Oldham, *Analytical Chemistry*, 1990, **62**,

1144–1147.

[204] N. H. Fontaine and T. E. Furtak, *J. Opt. Soc. Am. B*, 1997, **14**, 3342–3348.

[205] N. H. Fontaine and T. E. Furtak, *Phys. Rev. B*, 1998, **57**, 3807–3810.

[206] M. W. Meyer, V. H. Nguyen and E. A. Smith, *Vibrational Spectroscopy*, 2013, **65**, 94–100.

[207] H. Schwenke and J. Knoth, *Analytical Sciences*, 1995, **11**, 533–537.

[208] H. Schwenke, J. Knoth, R. Günther, G. Wiener and R. Bormann, *Spectrochimica Acta Part B: Atomic Spectroscopy*, 1997, **52**, 795–803.

[209] Y. Ohkata, T. Tsuno, E. Matsui, H. Takanashi and K. Itoh, *Chemical Physics Letters*, 1998, **295**, 17–24.

[210] Y. Nishikawa, T. Nakano and I. Noda, *Appl. Spectrosc.*, 2012, **66**, 312–318.

[211] K. Guha, *Ph.D. thesis*, Durham University, 2011.

[212] D. A. Beattie, S. Winget and C. D. Bain, *Tribology Letters*, 2007, **27**, 159–167.

[213] F. Mangolini, A. Rossi and N. Spencer, *Tribology Letters*, 2012, **45**, 207–218.

[214] P. M. Cann and H. A. Spikes, *Tribology Letters*, 2005, **19**, 289–297.

[215] S. Jiang, S. C. Bae and S. Granick, *Langmuir*, 2008, **24**, 1489–1494.

[216] P. M. Cann, *MRS Bulletin*, 2008, **33**, 1151–1158.

[217] X. H. Zhang, A. Quinn and W. A. Ducker, *Langmuir*, 2008, **24**, 4756–4764.